Dorso-Ventral and Night-Day Regulation of Extracellular K+ Dynamics in Mouse Hippocampal Astrocytes

Nariman KIANI[1‡✉], Kabeer ABUBAKAR[1‡], Tin Luka PETANJEK[2], Monique ESCLAPEZ[1,3], Anton IVANOV[1], and Christophe BERNARD[1✉]

[1] Aix Marseille Univ, INSERM, INS, Inst Neurosci Syst, Marseille, France

[2] University of Zagreb, Department of Physiology and Department of Neuroscience, Croatian Institute for Brain Research, School of Medicine, Zagreb, Croatia

[3] Aix Marseille Univ, Inserm, INMED, Institut de Neurobiologie de la Méditerranée, Marseille, France

‡ Equal contribution

✉ Corresponding authors

CONFLICT OF INTEREST

The authors declare that they have no conflict of interest.

DATA AVAILABILITY STATEMENT

The data that support the findings of this study are available from the corresponding author upon reasonable request.

Orchid IDs

Nariman KIANI : https://orcid.org/0009-0003-8809-0521
Kabeer ABUBAKAR : https://orcid.org/0000-0001-7552-0383
Tin Luka PETANJEK : https://orcid.org/0000-0002-8950-8315
Monique ESCLAPEZ : https://orcid.org/0000-0002-8558-1363
Anton IVANOV : https://orcid.org/0000-0001-8305-1062
Christophe BERNARD: https://orcid.org/0000-0003-3014-1966

Acknowledgements

This work was supported by the European Union's Horizon 2020 Research and Innovation Program under Grant Agreement Number 956325, the Fondation pour la Recherche Médicale (FRM) FDT202404018111, the Croatian Science Foundation under project number IP-2022-10-8493, and Petroleum Technology Development Fund (PTDF/ED/OSS/PHD/KA/2015/22).

Correspondence: Nariman KIANI, Christophe BERNARD
Université Aix-Marseille, INS, Inserm, UMR1106, Faculté de Médecine de la Timone
27 boulevard jean moulin 13385 MARSEILLE, France
Nariman.KIANI@univ-amu.fr, Christophe.BERNARD@univ-amu.fr

Abstract

Astrocytes regulate extracellular potassium (K^+) through multiple mechanisms operating across distinct spatiotemporal scales, yet whether this regulation exhibits regional and circadian specificity remains unclear. Using real-time K^+ measurements combined with electrophysiology and immunohistochemistry in astrocytes, we characterize K^+ buffering by astrocytes across the dorsoventral hippocampal axis at three circadian times. We report that hippocampal CA1 *stratum radiatum* astrocytes possess different functional K^+ buffering capacities depending on both anatomical location and time of day. At the early light phase (ZT3), the ventral hippocampus (VH) exhibits faster K^+ accumulation and greater peak amplitudes than the dorsal hippocampus (DH), despite similar neuronal network activity. This regional divergence is driven by reduced Kir4.1 channel function in VH astrocytes, which persists across all measured time points, and which is partially compensated by enhanced Na^+/K^+-ATPase activity specifically at ZT3. Gap junction coupling between astrocytes shows regional and time-dependent variation, with elevated coupling in VH at ZT3 that subsequently normalizes. Kir4.1 protein expression exhibits circadian dynamics, particularly in DH where expression declines from early light to late light and recovers in early dark. These findings establish astrocytic K^+ buffering as a multiscale phenomenon integrating regional heterogeneity with circadian regulation, with implications for understanding regional and temporal differences in network excitability, particularly in epilepsy.

Key words: Astrocytes, hippocampal regions, K+ homeostasis, Kir4.1 channels, circadian rhythm

55 **Introduction**

56 Under physiological conditions, extracellular K^+ concentration ($[K^+]_o$) fluctuates between 2
57 and 5 mM, while increases above 10 mM are linked to pathological activities such as
58 seizures and spreading depression (de Curtis et al., 2018; Enger et al., 2015; Erecińska &
59 Silver, 1994). Maintaining $[K^+]_o$ within narrow physiological limits is therefore functionally
60 important.

61 Astrocytes play an important role in regulating $[K^+]_o$ by taking up excess extracellular K^+,
62 redistributing it through gap-junction–connected networks, and extruding it where $[K^+]_o$ is
63 lower (Wallraff et al., 2006; Walz, 2000). This process relies on inward-rectifying Kir4.1
64 channels (Seifert et al., 2009), and the Na^+/K^+-ATPase pump. Impairment of either
65 component can increase neuronal and network activity and excitability (Djukic et al., 2007;
66 Romanos et al., 2020; Wallraff et al., 2006).

67 Neuronal activity and excitability are not uniform across the brain. Even within a single
68 structure, distinct subregions exhibit marked differences in intrinsic excitability, synaptic
69 properties, and responses to pharmacological or pathological challenges. For example,
70 along the dorsoventral axis of the hippocampus, the ventral region (VH) displays higher
71 intrinsic excitability, greater seizure susceptibility, distinct patterns of synaptic plasticity,
72 and different metabolic properties compared to the dorsal region (DH) (Brancati et al., 2021;
73 Dougherty et al., 2012; Papatheodoropoulos et al., 2005). Similarly, neuronal activity is not
74 constant across time: circadian rhythms modulate neuronal excitability, synaptic
75 transmission, and seizure threshold (B.-L. Chang et al., 2018; Debski et al., 2020; Quigg et

76 al., 2000), reflecting temporal regulation of molecular, metabolic, and physiological
77 processes (Brancati et al., 2021; Debski et al., 2020; McCauley et al., 2020).

78 This raises a fundamental question: do astrocytes exhibit similar spatial and temporal
79 heterogeneity in their K^+ buffering capacity? Do they "follow the pace" of neuronal activity,
80 adapting their homeostatic functions to match regional differences in excitability and
81 circadian variations in network state? If astrocytic K^+ buffering were spatially and temporally
82 invariant, regions of high neuronal excitability (such as the VH) and periods of elevated
83 seizure susceptibility (such as specific circadian phases) would be vulnerable to inadequate
84 K^+ homeostasis. Conversely, if astrocytes dynamically adjust their buffering capacity in
85 space and time, this could represent a sophisticated form of adaptive homeostasis
86 matched to local circuit demands.

87 The hippocampus provides an ideal system to address this question. Beyond the well-
88 documented differences in neuronal properties along the dorsoventral axis and across
89 circadian time, the hippocampus also exhibits regional and temporal heterogeneity in
90 astrocytic molecular markers, morphology, and calcium signaling (Dong et al., 2009; Jinno,
91 2011; Ryu et al., 2024; Thompson et al., 2008). However, whether these molecular and
92 morphological differences translate into functional differences in K^+ buffering—and how
93 they relate to the known regional and circadian variation in neuronal excitability—remains
94 unclear.

95 Here, we directly test whether astrocytic K^+ buffering capacity varies across the
96 dorsoventral hippocampal axis and across circadian time, using integrated functional,

electrophysiological, and molecular approaches. We use an extracellular K^+ sensor to measure K^+ dynamics during standardized synaptic stimulation (Schaffer collateral activation), monitoring multiple parameters of the K^+ transient (accumulation rate, peak amplitude, clearance kinetics, and Na^+/K^+-ATPase-dependent undershoot) in dorsal and ventral hippocampal slices at three Zeitgeber times: ZT3 (early light, baseline period), ZT8 (late light, period of heightened seizure susceptibility (W.-C. Chang et al., 2018; Debski et al., 2020; Quigg et al., 2000), and ZT15 (early dark, active phase). We then employ whole-cell patch-clamp electrophysiology to assess the cellular mechanisms underlying these functional differences, examining gap-junction coupling, Kir4.1 channel function, and astrocyte resting membrane potential. Finally, we use immunohistochemistry to quantify regional and circadian variation in Kir4.1 protein expression. Our findings demonstrate that astrocytic K^+ buffering capacity depends upon both anatomical location and circadian phase, revealing a form of adaptive heterogeneity that parallels—but does not simply mirror—the spatial and temporal organization of neuronal excitability.

Methods

Animals and Ethical Approval

All animal procedures were conducted in accordance with the European Directive 2010/63/EU and French regulations on animal experimentation. The study protocol was approved by the relevant institutional and national ethics committees (APAFIS authorization #44598-2023081812555435v4). A total of 50 male FVB mice (weight: 28–45 g; age: 2 months or older) were used. Of these, 3 mice were dedicated to immunohistochemistry, while the

118 remaining animals were used for both patch-clamp experiments and K^+ dynamic recordings
119 in parallel. The single-sex design increased statistical power and ensured an adequate yield
120 of viable samples given the technically demanding nature of the experiments. The exclusion
121 of female mice is a limitation of the study, and future work will be required to assess the
122 generalizability of these findings across sexes.

123 **Brain slice preparation**

124 Mice anesthetized with sevoflurane, were decapitated, and the brain was swiftly removed
125 from the skull and submerged in ice-cold artificial cerebrospinal fluid (ACSF) (in mM): NaCl
126 126, KCl 3.50, NaH_2PO_4 1.25, $NaHCO_3$ 25, $CaCl_2$ 2, $MgSO_4$1.3, and glucose 10, with a pH
127 value maintained between 7.3 and 7.4. The ACSF was aerated with a 95% O_2/5% CO_2 gas
128 mixture. One hemisphere, left or right in alternation, was used to prepare dorsal slices via
129 coronal sections, whereas the other hemisphere was used to prepare ventral slices as
130 described previously (Dougherty et al., 2012). The brain was immersed in an ice-cold cutting
131 solution (in mM): K-gluconate 140, HEPES 10, Na-gluconate 15, EGTA 0.2, and NaCl 4, with
132 the pH adjusted to 7.2 with KOH. Using a tissue slicer (Leica VT 1200s, Leica Microsystem,
133 Germany), 300 µm-thick for patch-clamp recording and 350 µm- thick slices for field
134 recording were produced. Subsequently, to preserve the cells near the surface from
135 resulting damage caused by slicing, the 300 µm-thick slices were incubated for 15 to 20
136 minutes at room temperature (RT) in a choline chloride solution (in mM): Choline Chloride
137 110, KCl 2.5, NaH_2PO_4 1.25, $MgCl_2$ 10, $CaCl_2$ 0.5, $NaHCO_3$ 25, Glucose 10, Na-Pyruvate 5,
138 constantly bubbled with a 95% O_2/5% CO_2 gas mixture. To label the astrocytes, the slices
139 were incubated for 20 minutes in a ACSF solution containing 1 µM of sulforhodamine 101

140 (SR101, Merk), a fluorescent dye specifically absorbed by astrocytes and not neurons
141 (Nimmerjahn et al., 2004). The slices were allowed to recover in a dual-side perfusion
142 holding chamber with continuously circulating ACSF for at least one hour before
143 experimentation.

144 **Synaptic stimulation and field potential recordings**

145 In parallel, 350 μm-thick transferred to a dual perfusion recording chamber continuously
146 perfused (~6 ml/min) with ACSF containing 5 mM of glucose, warmed to 30°C. Schaffer
147 collateral (SC) was stimulated with a bipolar metal electrode connected to a DS2A-isolated
148 stimulator (Digitimer Ltd, UK). The electrode tip was placed in the *Stratum Radiatum* (*s.r.*)
149 between the CA3 and CA2 regions. Extracellular recording electrodes were pulled (Harvard
150 Apparatus Ltd, UK , O.D. = 1.2 and I.D. = 0.94 mm, Rp < 1 MΩ) using a horizontal puller (Sutter
151 Instruments, USA). The extracellular local field potential (LFP) was recorded with a glass
152 microelectrode filled with ACSF, placed in the *Stratum Oriens* (*s.o.*) towards the *Stratum*
153 *Pyramidale* (*s.p.*) of the CA1 area. The signal was amplified 1000 times with an EXT-02F
154 amplifier (NPI Electronic, Germany) operating with a low-pass 3kHz filter (DC mode). The
155 stimulation current intensity was adjusted to produce an LFP response of 60-70% of the
156 maximum amplitude. Each slice was stimulated with trains of stimulation pulses of different
157 frequencies ranging from 2.5Hz to 100Hz. The LFP responses were recorded simultaneously
158 with the K^+-dependent potential using Patch Master software. Each stimulation protocol
159 was repeated twice. The LFP responses to single pulse stimulation were monitored in
160 between train stimulations to check the slice stability. If the response decreased by more
161 than 20%, the slice was discarded. In this study, we used the response to the 10Hz30s trains

162 because this stimulation evoked a K^+ signal with good SNR, allowing the measurement of
163 required parameters (peak amplitude, 25-75% rise time, decay time, and undershoot
164 amplitude) of the individual and not the averaged response.

165 **Fabrication of Potassium Sensitive Microelectrode**

166 K+-selective microelectrodes were prepared using the method described by Heinemann
167 and Arens (1992). In brief, electrodes were pulled from double-barrel theta glass (TG150-4,
168 Warner Instruments, Hamden, CT, USA). The reference barrel was filled with 154 mmol/L
169 NaCl solution. The silanized ion-sensitive barrel tip (5% trimethyl-1-chlorosilane in
170 dichloromethane) was filled with a potassium ionophore I cocktail A (60031 Fluka
171 distributed by Sigma-Aldrich, Lyon, France) and backfilled with 100 mmol/L KCl.
172 Measurements of K^+-dependent potentials were performed using a high-impedance
173 differential DC amplifier equipped with negative capacitance feedback control, which
174 permitted the compensation of the microelectrode capacitance required for the recording
175 of the rapid changes of $[K^+]_o$. The electrodes were calibrated before each experiment. The
176 calibration curve, concentration vs potential, was fitted with an exponential function. The
177 obtained equation was used to convert $[K^+]_o$-dependent potential recordings into
178 concentration changes.

179 **Electrophysiological recording of the astrocytes**

180 For the electrophysiological recordings of astrocytes, 300 µm-thick slices were immersed in
181 a low-volume (2 ml) recording chamber and continuously perfused with ACSF at 32 - 34°C
182 and a perfusion rate of 5 mL/min. Sulforhodamine labeled astrocytes in the *stratum*

183 *radiatum* (*s.r.*) of the CA1 region of the hippocampus were identified as a fluorescent cells
184 with astrocytic morphology (excitation/emission wavelengths of 586/605 nm). Patch
185 pipettes were fabricated using the same horizontal puller from borosilicate glass tubing
186 (Harvard Apparatus Ltd, UK ,1.5 mm outer diameter (O.D.), 0.86 mm inner diameter (I.D.),
187 pipette resistance (Rp) = 5.78 ± 0.12 MΩ) and filled with an intrapipette solution (in mM): KCl
188 20, K-gluconate 115, HEPES 10, EGTA 1.1, MgATP 4, Na -phosphocreatine 10, Na_2GTP 0.4,
189 and 0.3-0.4% biocytin (Sigma, Germany). Signals were transmitted to a Multiclamp 700A
190 amplifier (Molecular Devices), digitized at a rate of 10 kHz using a DigiData 1550 interface
191 (Molecular Devices) connected to a personal computer, and analyzed using ClampFit
192 software (Molecular Devices). The resting membrane potential (RMP) of astrocytes was
193 measured using the patch-clamp technique, whole-cell configuration, in current clamp
194 mode.

195 **Isolation of Kir4.1 currents**

196 To isolate Kir4.1 currents and to keep constant the extracellular K^+, slices were incubated
197 for 36 ± 2 minutes in the baseline 5 mM glucose-containing ACSF supplemented with (in
198 μM): Meclofenamic acid (MFA, Sigma-Aldrich) 100 to block gap junctions, and Tetrodotoxin
199 (TTX, Abcam) 0.5, 6-Cyano-7-nitroquinoxaline-2,3-dione (CNQX, HelloBio) 10, and D-(-)-2-
200 Amino-5-phosphonopentanoic acid (D-AP5, HelloBio) 40 to stop neuronal firing and
201 minimize synaptic transmission. No effect of incubation time on Kir4.1 current was
202 detected. Upon establishment of the whole-cell patch clamp configuration, the patched
203 astrocyte was held at -70 mV in voltage clamp mode, and after 5 minutes of dialysis,
204 membrane currents were recorded at different holding potentials varying from -140mV to

205 50mV with 10mV steps. Then, to block Kir4.1 channels, 100 μM of $BaCl_2$ was added to the
206 baseline ACSF, and the currents elicited by the same voltage steps were recorded after 5
207 minutes. The current-voltage relationship of Ba^{2+} sensitive conductance was determined by
208 subtracting the currents recorded in Ba^{2+} from those recorded before its administration.
209 Access resistance was determined by biexponentially fitting the capacitive current resulting
210 from −70 to −60 mV voltage step. Cells were discarded if they met any of the following
211 criteria: an initial access resistance above 35 MΩ, a resting membrane potential (RMP) less
212 negative than -50 mV, or a final access resistance increase of more than 20%.

213 **Coupling estimation**

214 Astrocytes are extensively coupled via gap junctions formed by Cx43 and Cx30, supporting
215 intercellular redistribution of ions and metabolites, including potassium buffering.
216 Pharmacological inhibition of these gap junctions is expected to uncouple astrocytes and
217 thereby reducing their capacity for spatial potassium buffering. In principle, comparing K^+-
218 dependent currents evoked by Schaffer collateral stimulation before and after gap junction
219 blockade could provide an estimate of the coupling state of the recorded astrocyte.

220 However, available gap junction inhibitors lack specificity and profoundly affect neuronal
221 and glial function. Carbenoxolone alters both AMPA and $GABA_A$ receptor-mediated synaptic
222 transmission (Tovar et al., 2009). Meclofenamic acid is a potent activator of KCNQ2/Q3
223 (Kv7.2/7.3, M-type) channels (U. A. Anderson et al., 2009). and, at the 50–100 μM
224 concentrations commonly used to block gap junctions, hyperpolarizes CA1 neurons and
225 suppresses synaptic responses (Peretz et al., 2005). Connexin mimetic peptides such as

226 Gap26 and Gap27, while they are more specific at the channel level, also reduce basal
227 excitatory synaptic transmission, likely by inhibiting gliotransmitter release through Cx43
228 hemichannels (Dospinescu et al., 2025). Because all of these agents can alter overall
229 network activity, they inevitably affect not only K+ buffering but also activity-dependent K+
230 release. To avoid these confounding effects, we adopted an alternative approach to assess
231 astrocytic coupling, based on the spread of the gap junction–permeable intracellular tracer
232 biocytin following controlled whole-cell loading (Stephan et al., 2021).

233 In a separate set of experiments, astrocytes were patched in the absence of any blocker in
234 whole cell configuration and kept at -70 mV holding potential for 20 mins. Slices were then
235 fixed in 4% paraformaldehyde (AntigenFix, Diapath) overnight at 4°C. After three 30-minute
236 washes in 0.12 M phosphate buffer (PB), slices were cryoprotected in 20% sucrose
237 overnight, then deep-frozen on dry ice and stored at -80°C until the day of experimentation.

238 To reveal biocytin-containing astrocytes, slices were rinsed in PB twice, in 0.02 M potassium
239 phosphate buffered saline (KPBS) three times for 30 min, and then incubated with
240 streptavidin-conjugated with fluorophore Alexa 488 (Abcam) diluted (1/200) in KPBS
241 containing 0.3% Triton-X100, overnight at RT. After washing with KPBS for 3 x 30 min, slices
242 were mounted on Superfrost™ slides using Fluoromount-G.

243 To visualize the stained astrocytes coupling, slices were imaged using a Zeiss LSM 700
244 inverted confocal microscope with a 20x (0.5x zoom) objective. Z-stacks (15–35 optical
245 slices, length: 2048 pixels, width: 2048; 1 µm interval) were acquired in the CA1 *stratum*

246 *radiatum* using Zeiss ZEN software. Z-stacks were merged using Fiji software (NIH), and pixel
247 intensity was then normalized.

248 A blinded examiner then counted the number of stained astrocytes. Since only one astrocyte
249 per slice was patched, the stained astrocytes were mandatory, those connected with the
250 patched one directly or through other connected astrocytes. Therefore, we considered the
251 number of stained astrocytes as an estimation of the astrocytic coupling.

252 **Immunohistochemistry and image analysis**

253 ***Tissue preparation, Immunohistochemistry, and image analysis***

254 Wild-type male FVB mice (P50–70) were anesthetized with an intraperitoneal injection of
255 ketamine and xylazine, followed by a lethal dose of pentobarbital administered at
256 designated Zeitgeber times (ZT3, ZT8, or ZT15). Mice were then transcardially perfused with
257 cold 0.12 M PB to remove the blood and then with AntigenFix to fix the tissue. Brains were
258 extracted, post-fixed for up to 4 hours in the same fixative, rinsed in PB, cryoprotected in
259 20% sucrose in PB overnight at 4°C, quickly frozen on dry ice and kept at -80°C. Hemisected
260 blocks of brain containing dorsal and ventral hippocampus were sectioned at 40 µm using
261 a cryostat. The Sections were collected sequentially in tubes containing an ethylene glycol-
262 based cryoprotective solution (Lu & Haber, 1992; Watson et al., 1986) and stored at –20°C
263 until histological processing.

264 ***Double labeling for GFAP and Kir4.1***

265 Sections were processed for the simultaneous detection of GFAP to label astrocytes and
266 the Kir4.1 channel. They were rinsed for 30 min in PB and for 2x30 mins in KPBS. Sections
267 were then incubated for 1h at RT in 3% normal donkey serum (NDS) diluted in KPBS
268 containing 0.3% Triton X-100 and overnight at RT in a solution containing the polyclonal
269 guinea pig anti -GFAP (1:600, #AFP-001-GP, Alomone Labs) and polyclonal rabbit anti-Kir4.1
270 (1:500, #APC-035, Alomone Labs) diluted in KPBS containing 0.3% Triton X-100 and 1% NDS.
271 After 3, 30-minute rinses in KPBS, sections were incubated for 2 h in Alexa Fluor 488-
272 conjugated donkey anti-guinea pig IgG (1:100, #706-545-148, Jackson ImmunoResearch)
273 and Cy3-conjugated donkey anti-rabbit IgG (1:100, #711-167-003, Jackson
274 ImmunoResearch), diluted in KPBS and 3% NDS. Sections were then rinsed with 3x30 rinses
275 of KPBS and mounted on Superfrost™ slides using Fluoromount-G containing the nuclear
276 marker DAPI (Thermo Fisher).

277 Immunofluorescence was imaged on a Zeiss LSM 700 inverted confocal microscope using
278 a 63x oil-immersion objective. Z-stacks (12–19 optical slices at 1 μm intervals) of the CA1
279 *stratum radiatum* were acquired using Zeiss ZEN software. One field of view per section was
280 imaged. Z-projections were performed in Fiji (NIH), and GFAP signal was quantified by
281 measuring its integrated density. Thereafter, the GFAP was thresholded using triangle
282 method, creating a mask that defined the region of interest (ROI) for Kir4.1 analysis. Then,
283 Kir4.1 signal within the GFAP-defined ROI was quantified using the AND operation in the
284 Image Calculator, and the Kir4.1/GFAP integrated density ratio was calculated (Bataveljic et
285 al., 2024).

286 **Statistical analysis**

Statistical analyses were performed using R software (version 4.5.1). K^+ transient parameters were all normalized to that of DH at ZT3, and subsequent analyses were performed on these normalized data. To provide a comprehensive analysis of the data, we used two different approaches: permutation-based hypothesis testing to identify significant main effects and Bayesian multilevel modeling to estimate the magnitude and uncertainty of those effects.

Permutation-Based Hypothesis Testing

Analyses involving the effects of region (DH vs. VH) and time (ZT3, ZT8, and ZT15) were performed using a resampling-based, Freedman-Lane permutation ANOVA from the permuco package in R (Kherad-Pajouh & Renaud, 2015). This non-parametric approach was selected to provide robust inference by reducing assumptions about data distribution—such as normality and sphericity. The analysis was conducted with 10,000 permutations to ensure stable p-value estimates. Effect sizes were calculated and reported as omega squared (ω^2), which represents the proportion of variance in the tested parameter accounted for by each effect in the population. The magnitude of regional differences was also evaluated using an online estimation statistics tool, which reported the mean difference and corresponding 95% confidence intervals (Ho et al., 2019).

Bayesian Multilevel Modeling

To further analyze the effects of region, time, and their interactions while accounting for the hierarchical structure of our experimental design (e.g., multiple cells nested within animals), we performed Bayesian multilevel modeling using the brms package (version

2.22.0) (Bürkner, 2017). This framework allowed us to move beyond binary significance testing to provide a probabilistic estimation of parameter uncertainty. Models were specified with fixed effects for region, timepoint, and their interaction.

We used the fitdistrplus package (version 1.2.4) to identify the optimal family distribution for each variable based on the lowest Akaike Information Criterion (AIC), ensuring the model accurately reflected the data's underlying structure (Delignette-Muller & Dutang, 2015). Four independent Markov Chain Monte Carlo (MCMC) chains were run with 4,000 iterations each (2,000 warm-up); convergence was confirmed via $\hat{R} < 1.01$ and sufficiently high effective sample sizes. Parameter estimates are reported as posterior medians with 95% credible intervals (CrI). Predictors were centered and scaled where appropriate to aid convergence.

Results

Extracellular K+ dynamics exhibit regional and circadian specificity

We first characterized how extracellular ($[K^+]_o$) concentration changes in the hippocampus during and after standardized neuronal network activity, examining whether these dynamics differ between dorsal and ventral hippocampus across circadian time. We used a 10 Hz, 30-second stimulation of Schaffer collaterals to evoke robust $[K^+]_o$ release from activated neurons (Fig. 1A and B). This protocol was selected to ensure that the neuronal network response reached true peak amplitude and steady state before stimulus termination, enabling consistent comparison across experimental groups (see Methods).

Synaptic strength is comparable across space and time

329 To ensure valid comparisons of $[K^+]_o$ transient properties, we first verified that evoked
330 neuronal activity was equivalent between regions and time points. The magnitude of the
331 local field potential (LFP) integral served as a quantitative proxy for network response
332 intensity. Statistical analysis revealed no significant effects of hippocampal region (DH
333 versus VH), Zeitgeber time (ZT), or their interaction on evoked LFP strength (Fig. 1C). This
334 uniformity confirms the robustness of our stimulation paradigm and validates the
335 assumption that any observed differences in $[K^+]_o$ dynamics reflect astrocyte properties
336 rather than variations in neuronal input.

337 **Ventral hippocampus accumulates $[K^+]_o$ more rapidly and to greater amplitudes,**
338 **particularly at early light phase**

339 We assessed $[K^+]_o$ accumulation by analyzing the peak amplitude of $[K^+]_o$ transients.
340 Permutation analysis of variance (ANOVA) shows a significant main effect of the regions only
341 ($F(1, 98) = 12.05$, *permutation p* = .0010, $\omega^2 = 0.0950$), where the pool of VH samples shows
342 65% [95%CI 26%, 101%] larger $[K^+]_o$ peak amplitude than DH ones. Bayesian regression
343 confirmed that this difference is predominantly driven by ZT3. At this time point, $[K^+]_o$ in the
344 VH was 105% higher than in the DH [95% CrI: 40.5% , 200.4%]. In contrast, at ZT15, the DH
345 exhibited a peak amplitude that was 71.6% greater than at ZT3 [95% CrI: 17.4% , 150.9%],
346 suggesting that the transition from ZT3 (light cycle) to ZT15 (dark cycle) promotes greater
347 $[K^+]_o$ accumulation in the DH (Fig. 1D).

348 Analysis of the slope of the 25–75% rise phase of $[K^+]_o$ transients revealed that VH reached
349 peak $[K^+]_o$ 305.5% faster than the DH [95% CI: 124.8%, 646.3%] at ZT3. In the DH, the

350 transition from ZT3 to ZT8 produced no clear change [27.1%, 95% CrI: −26.7%, 120.3%],
351 whereas the transition to ZT15 resulted in a substantial increase in accumulation rate
352 [122.6%, 95% CrI: 28.4%, 293.5%]. Importantly, the regional advantage of the VH diminished
353 at later time points. Relative to its ZT3, the VH effect was attenuated by 41.7% at ZT8 [95%
354 CrI: 19.0%, 93.1%] and by 33.3% at ZT15 [95% CrI: 14.9%, 72.7%], confirming a significant,
355 negative interaction between region and time. (Fig. 1E).

356 Collectively, these results demonstrate that comparable neuronal network activity
357 produces different extracellular $[K^+]_o$ dynamics between dorsal and ventral hippocampus,
358 suggesting regional differences in astrocytic K^+ buffering capacity. This regional divergence
359 is most pronounced at the early light phase.

360 **$[K^+]_o$ clearance kinetics show similar rates despite regional differences in**
361 **accumulation**

362 To distinguish whether faster $[K^+]_o$ accumulation in VH reflects impaired $[K^+]_o$ removal or
363 differential regulation at the rising phase of activity, we analyzed $[K^+]_o$ decay kinetics by
364 fitting monoexponential decay (τ_{decay}) to the falling phase of the transient. Permutation
365 ANOVA revealed a significant main effect of region ($F(1, 98) = 3.93$, permutation $p = 0.0496$,
366 $\omega^2 = 0.0278$), with VH showing an overall 14.5% faster decay than DH [95% CI: -0.20%,
367 28.1%]. However, Bayesian regression analysis incorporating temporal variation did not
368 identify statistically robust regional differences across time points. When analyzed within
369 specific circadian phases, differences were modest and credible intervals crossed zero: at
370 ZT3, DH exhibited 22.3% slower decay than VH [95% CrI: -5.9%, 50.2%]; at ZT8 and ZT15,

371 differences were 15.2% [95% CrI: -14%, 41.5%] and 17.0% [95% CrI: -11%, 42.1%],
372 respectively (Fig. 1F).

373 This paradoxical finding – accelerated $[K^+]_o$ accumulation in VH despite similar or faster
374 clearance rates – indicates that differential $[K^+]_o$ dynamics are driven by regional difference
375 at the rising phase of the transient rather than the decay phase, suggesting that distinct
376 buffering mechanisms may be preferentially engaged during accumulation versus recovery.

377 **Ventral hippocampus displays enhanced putative Na^+/K^+-ATPase activity specifically**
378 **at early light phase**

379 The similar decay kinetics between regions despite higher $[K^+]_o$ accumulation in VH
380 prompted us to examine the recovery phase. After prolonged stimulation (10 Hz, 30 s), $[K^+]_o$
381 return to baseline is followed by an undershoot (Fig. 1B, right panel, black arrows), a
382 transient decrease of K^+ concentration below baseline level that reflects Na^+/K^+-ATPase
383 activity (Chever et al., 2010; D'Ambrosio et al., 2002). Analysis of undershoot amplitude
384 revealed significant regional effects and complex temporal dynamics: permutation ANOVA
385 revealed a significant effect of region ($F(1, 105) = 26.65$, permutation $p = 0.0001$, $\omega^2 = 0.180$)
386 as well as significant interaction of time with region ($F(2, 105) = 3.074$, permutation $p =$
387 0.0482 , $\omega^2 = 0.0290$). Bayesian regression analysis revealed that at ZT3, VH showed a 239%
388 increase in undershoot amplitude compared to DH [95% CrI: 54%, 624%]. While VH
389 maintained elevated undershoot amplitudes at ZT8 and ZT15, the magnitude of this regional
390 difference was attenuated at these later timepoints [ZT8: -49%, 95% CrI: -82% , +42%; ZT15:
391 -48%, 95% CrI: -81% , +48%] (Fig. 1G).

392 These findings suggest that VH astrocytes display enhanced Na^+/K^+-ATPase activity,
393 particularly pronounced at the early light phase. Despite this elevated pump activity, overall
394 $[K^+]_o$ clearance rates remain unchanged, suggesting that the enhanced pump activity
395 primarily reflects the greater $[K^+]_o$ accumulation in VH (which provides greater driving force
396 for pump activation) rather than fundamentally altering the rate constant of $[K^+]_o$ removal.
397 This raises the question: what cellular mechanisms limit $[K^+]_o$ buffering capacity in the
398 ventral hippocampus?

399 **Cellular basis of regional $[K^+]_o$ buffering differences: a role for reduced Kir4.1 function**
400 **in ventral astrocytes**

401 **Astrocytic Gap Junction Coupling Shows Regional and Temporal Variation**

402 Potassium redistribution through astrocytic networks depends on gap junction-mediated
403 coupling, which expands the effective volume available for $[K^+]_o$ uptake. We examined
404 whether astrocytic coupling—measured by quantifying the number of biocytin-labeled cells
405 connected to a patched astrocyte—exhibits regional and circadian variation (Fig. 2A).
406 Across all time points, VH slices showed a trend toward more coupled astrocytes than DH
407 [mean difference: 13 cells, 95% CI: -4, 30], but this difference did not reach statistical
408 significance in permutation ANOVA ($F(2, 63) = 2.75$, permutation $p = 0.0686$, $\omega^2 = 0.0483$).
409 However, Bayesian regression analysis revealed significant regional and temporal effects.
410 Specifically, at ZT3, VH slices exhibited 39 more coupled cells than DH [95% CrI: +15 , +69],
411 corresponding to a 36.3% increase [95% CrI: 8.3% , 70.0%]. This regional difference was

412 absent at ZT8. At ZT15, DH coupling increased by 27% compared to its ZT3 value [95% CrI:
413 1% , 60%], while VH coupling declined by 16.2% [95% CI: 6.8% , 52.3%] (Fig. 2A and B).

414 Enhanced gap junction coupling in VH at ZT3 would be expected to facilitate $[K^+]_o$
415 redistribution and thus improve buffering capacity. The fact that VH nevertheless shows
416 greater $[K^+]_o$ accumulation at this timepoint suggests that reduced K^+ conductance
417 mechanisms (rather than impaired redistribution) are the primary determinant of regional
418 differences.

419 **Ventral hippocampal astrocytes display reduced Kir4.1-mediated conductance across**
420 **all circadian phases**

421 Kir4.1 channels mediate the primary K^+-dependent astrocytic conductance and are central
422 to spatial buffering, particularly during the rising phase of $[K^+]_o$ transients when astrocytic
423 depolarization drives K^+ influx through these channels (Larsen et al., 2014; Seifert et al.,
424 2009). To directly assess Kir4.1 function, we performed whole-cell patch-clamp recordings
425 (Fig. 3A) in the presence of gap junction blocker (MFA) and neuronal transmission blockers
426 (TTX, CNQX, D-AP5), isolating Kir4.1-specific currents via subsequent Ba^{2+} application
427 (Wallraff et al., 2006). Indeed, application of MFA was demonstrated to be effective in
428 uncoupling astrocytes, as shown by the number of dye-coupled cells (Fig. 3B-C).

429 Resting membrane potential did not vary significantly between regions or across time (Fig.
430 3D). Application of Ba^{2+} caused an average depolarization of 5.5 ± 0.64 mV consistent with
431 blockade of inward-rectifying currents, confirming effective channel blockade. Permutation
432 ANOVA revealed a significant main effect of region on Ba^{2+}-induced depolarization (F(1, 43)

433 = 8.26, permutation p = 0.0051, ω^2 = 0.124), with DH astrocytes depolarizing 3.2 mV more
434 than VH astrocytes following Ba^{2+} application [95% CI: 0.90, 5.70], indicating higher
435 functional Kir4.1 expression in DH (Fig. 3E).

436 To more directly quantify Kir4.1-mediated conductance, we analyzed Ba^{2+}-sensitive current
437 at -130 mV holding potential, a voltage optimal for Kir4.1 channel activity (Seifert et al.,
438 2009). Permutation ANOVA revealed a significant effect of region (F(1, 43) = 13.30,
439 permutation p = 0.0006, ω^2 = 0.209). Bayesian regression confirmed a significant main effect
440 of region, with no effect of time or region-time interaction. On average, Ba^{2+}-sensitive
441 conductance represents 29% of total transmembrane current in DH astrocytes compared
442 to 17% in VH, with a mean difference of 12% [95% CI: 5.8% , 17.6%] (Fig. 3F-G). This
443 reduction in functional Kir4.1 conductance in VH relative to DH persists across all examined
444 circadian phases, suggesting that regional differences in Kir4.1 function are stable
445 properties of these astrocytes rather than acutely regulated.

446 This reduced Kir4.1-mediated conductance in VH astrocytes provides a mechanistic
447 explanation for the observed rapid and pronounced K^+ accumulation in this region: with
448 lower K^+ conductance, astrocytes can passively take up less K^+ in response to
449 depolarization, resulting in higher $[K^+]_o$ despite the presence of enhanced gap junction
450 coupling that could support redistribution.

451 We noticed that in some astrocytes the IV relationship of Ba^{2+}-sensitive current was linear
452 without rectification. We checked whether such astrocytes are more frequent in one of the
453 explored regions. Current rectification was assessed by dividing I-V curve slopes between –

454 140 to –90 mV by that of 0 to +50 mV voltage ranges. Cells with slope ratios >1 were classified
455 as rectifying. Fisher's exact test revealed no statistically significant association between
456 region and rectification status ($p = 0.104$), though the estimated odds ratio of 0.28 [95% CI:
457 0.04, 1.31] suggested a non-significant trend toward greater rectification in DH astrocytes
458 (Fig. 3H). Our findings indicate that Kir4.1-mediated currents are regionally regulated, with
459 higher functional expression in the DH compared to VH but are not modulated by circadian
460 time under these experimental conditions. This difference partly explains why, at the same
461 rate of potassium release, its accumulation is faster and greater in VH than in DH.

462 **Kir4.1 protein expression exhibits circadian dynamics distinct between dorsal and**
463 **ventral hippocampus**

464 To investigate whether regional differences in Kir4.1 current reflect corresponding
465 differences in protein abundance, and to assess circadian regulation of Kir4.1 expression,
466 we performed double immunolabeling for GFAP (astrocyte marker) and Kir4.1 on
467 hippocampal sections across the regions (Fig. 4A-B) as well as time points.

468 Analysis of GFAP-positive area fraction revealed a main effect of region ($F(1, 62) = 13.48$,
469 permutation $p = 0.0009$, $\omega^2 = 0.157$), although Bayesian analysis detected no statistically
470 robust effects (Fig. 4C). To account for regional differences in astrocytic Kir4.1 expression,
471 Kir4.1 integrated density was normalized to GFAP-positive area (astrocyte-specific
472 quantification). Values were further normalized within each immunolabeling batch to DH
473 samples to control batch variability.

474 Permutation ANOVA revealed a significant region × time interaction ($F(2, 62) = 4.14$,
475 permutation $p = 0.0119$, $\omega^2 = 0.092$). Bayesian regression analysis revealed nuanced
476 circadian regulation: at ZT3 (early light), DH showed significantly higher Kir4.1 levels than VH
477 [39.3% increase, 95% CrI: 14.8%, 56.8%]. The transition from ZT3 to ZT8 (late light) was
478 marked by significant decline in DH Kir4.1 expression [34.3% decrease, 95% CrI: 10.4%,
479 51.8%], whereas VH showed the opposite pattern with a 24.4% increase [95% CrI: 22.1%,
480 197.4%], resulting in substantial convergence of expression levels. No reliable regional
481 differences were detected at ZT15 (early dark) (Fig. 4D).

482 Importantly, these circadian changes in Kir4.1 protein abundance do not translate into
483 circadian modulation of Kir4.1-mediated currents (which showed only regional, not
484 temporal, variation in functional assays). This dissociation between protein expression
485 dynamics and current magnitude suggests complex post-translational regulation of Kir4.1
486 channel function.

487 **Integration and mechanistic synthesis**

488 Our results reveal a multiscale organizational principle for astrocytic K^+ buffering in
489 hippocampus: regional and circadian factors converge to determine buffering capacity
490 through complementary mechanisms operating at different phases of $[K^+]_o$ transients (Fig.
491 5).

492 At the early light phase (ZT3), the ventral hippocampus exhibits a state of heightened
493 extracellular K^+ accumulation characterized by: 1) reduced Kir4.1-mediated K^+
494 conductance (41% lower than DH) that persists across all times, 2) enhanced gap junction

495 coupling (35% more coupled astrocytes) that could support redistribution, 3) elevated
496 Na^+/K^+-ATPase-dependent undershoot (239% greater than DH) indicating compensatory
497 pump activation. These properties produce rapid and pronounced $[K^+]_o$ accumulation
498 despite the presence of potentially advantageous gap junction coupling. The putative
499 enhanced Na^+/K^+-ATPase activity likely reflects activation by the greater local $[K^+]_o$
500 accumulation and astrocytic depolarization, coupled with potentially higher pump
501 expression. Thus, at ZT3, ventral astrocytes are limited in their capacity to prevent $[K^+]_o$
502 accumulation during the rising phase.

503 As the circadian cycle progresses through the light phase (ZT3 to ZT8 to ZT15): 1) Kir4.1
504 protein expression increases in VH and decreases in DH, partially equalizing regional
505 differences by ZT15, 2) gap junction coupling normalizes between regions, 3) Na^+/K^+-ATPase
506 compensatory activity diminishes.

507 By the early dark phase (ZT15), the circadian pattern reverses, with DH $[K^+]_o$ accumulation
508 increasing relative to ZT3, suggesting that dorsal hippocampal astrocytes are subject to
509 time-dependent suppression of buffering capacity during the light phase, with restoration
510 during the dark phase. The nature of this circadian suppression remains to be determined
511 but may reflect circadian regulation of Kir4.1 trafficking or channel modulation by clock-
512 controlled signaling pathways.

513 **Discussion**

514 This study addresses the question of spatial and temporal heterogeneity in astrocytic
515 function. Using integrated functional, electrophysiological, and molecular approaches, we

516 demonstrate that astrocytic K^+ buffering in the hippocampus is jointly regulated by regional
517 identity and circadian phase, with important implications for understanding network
518 excitability, seizure susceptibility, and the temporal organization of brain states.

519 **Astrocytes show regional specialization but do not simply mirror neuronal excitability**
520 **patterns**

521 Our findings reveal that ventral hippocampal astrocytes possess fundamentally different
522 $[K^+]_o$ buffering properties compared to their dorsal counterparts. At the early light phase
523 (ZT3), when regional differences are most pronounced, VH accumulates $[K^+]_o$ more rapidly
524 and to higher peak amplitudes than DH despite equivalent neuronal network activity. This
525 regional divergence reflects intrinsic differences in astrocyte physiology rather than
526 variations in neuronal input, establishing that astrocytic heterogeneity is a primary
527 organizational principle of hippocampal circuits.

528 However, astrocytic regional specialization does not simply track neuronal excitability in a
529 compensatory manner. The VH is known to exhibit higher intrinsic neuronal excitability and
530 greater seizure susceptibility than the DH (Debski et al., 2020; Dougherty et al., 2012;
531 Papatheodoropoulos et al., 2005). If astrocytes were optimized to compensate for regional
532 differences in neuronal activity, one would predict enhanced $[K^+]_o$ buffering capacity in VH
533 to counterbalance its elevated excitability. Instead, we observe the opposite: VH astrocytes
534 display reduced Kir4.1-mediated conductance (12% lower than DH), resulting in greater
535 $[K^+]_o$ accumulation during neuronal activity. This counterintuitive arrangement suggests that
536 astrocytic properties are not configured to suppress regional differences in excitability but

537 rather may amplify or enable them, supporting the functionally distinct roles mediated by
538 dorsal and ventral hippocampus in cognition and behavior.

539 **The paradox of enhanced accumulation with preserved clearance: differential**
540 **mechanisms at rising vs. falling phases**

541 A central finding of this study is the paradoxical observation that VH exhibits both faster $[K^+]_o$
542 accumulation and similar (or slightly faster) clearance rates compared to DH. This apparent
543 contradiction is resolved by recognizing that distinct buffering mechanisms dominate during
544 different phases of the K^+ transient, with Kir4.1 channels playing a central role during
545 accumulation and Na^+/K^+-ATPase predominating during recovery.

546 In this study, Na^+/K^+ ATPase activity was quantified using the amplitude of the post-stimulus
547 K^+ undershoot rather than by pharmacological pump inhibition because it does not
548 selectively reduce $[K^+]_o$ clearance. Indeed, the pump inhibition depolarizes neurons, alters
549 firing patterns, and modifies synaptic transmission (T. R. Anderson et al., 2010), thereby
550 changing K+ release during Schaffer collateral stimulation. Consequently, $[K^+]_o$ transients
551 recorded after pump blockade reflect a mixture of impaired clearance and altered K^+
552 release, which cannot be disentangled. In contrast, the $[K^+]_o$ undershoot that follows a
553 defined activation epoch arises from activity-dependent stimulation of the Na^+/K^+ ATPase
554 and reflects the excess pump-mediated uptake of K^+ once neuronal firing has ceased. For
555 these reasons, undershoot analysis offers a more specific and interpretable functional
556 measure of Na^+/K^+ ATPase activity in our experimental condition.

557 During the rising phase of neuronal activity, when K^+ is actively released from depolarizing
558 neurons, $[K^+]_o$ elevation depolarizes nearby astrocytes, driving passive K^+ influx through
559 Kir4.1 channels down the electrochemical gradient (Larsen & MacAulay, 2014). This Kir4.1-
560 mediated uptake represents the fastest way to limit $[K^+]_o$ accumulation. Our
561 electrophysiological data demonstrate that VH astrocytes possess significantly reduced
562 Ba^{2+}-sensitive (Kir4.1-mediated) conductance compared to DH astrocytes, a decrease that
563 persists across all circadian phases examined. This reduced conductance directly explains
564 why VH accumulates $[K^+]_o$ more rapidly: with fewer functional Kir4.1 channels, astrocytes
565 cannot buffer K^+ as efficiently during the rising phase, resulting in higher extracellular
566 concentrations.

567 In contrast, during the decay phase after neuronal activity ceases, $[K^+]_o$ clearance is
568 dominated by active Na^+/K^+-ATPase pumping rather than passive Kir4.1-mediated influx
569 (D'Ambrosio et al., 2002; MacAulay, 2020). Our observation that VH exhibits a dramatically
570 enhanced $[K^+]_o$ undershoot (239% larger than DH at ZT3)—a signature of robust Na^+/K^+-
571 ATPase activity—indicates that pump-mediated clearance is elevated in VH. Importantly,
572 this enhanced pump activity likely reflects a compensatory response to the greater $[K^+]_o$
573 accumulation itself: higher $[K^+]_o$ and greater astrocytic depolarization both stimulate
574 Na^+/K^+-ATPase activity (Wang et al., 2012). Thus, the similar decay kinetics between regions
575 emerge not from equivalent intrinsic clearance capacity but from activity-dependent
576 upregulation of pumping in VH that compensates for its reduced Kir4.1 function.

577 This mechanistic model—reduced Kir4.1-mediated uptake during accumulation,
578 compensated by enhanced pump-mediated clearance during recovery—reconciles the

579 paradoxical K^+ dynamics and highlights the phase-specific contributions of different
580 buffering mechanisms.

581 **Gap junction coupling: enhanced connectivity cannot overcome reduced conductance**

582 An unexpected finding was that VH astrocytes exhibit enhanced gap junction coupling at ZT3
583 (35% more coupled cells than DH), precisely when and where K^+ accumulation is greatest.
584 At first glance, this enhanced coupling appears maladaptive: expanded astrocytic networks
585 should increase the effective volume available for K^+ redistribution and thus improve
586 buffering capacity (Wallraff et al., 2006). Yet VH accumulates more $[K^+]_o$.

587 This paradox highlights an important distinction between network connectivity (assessed by
588 gap junction coupling) and cellular K^+ conductance (determined primarily by Kir4.1
589 expression). Enhanced coupling expands the astrocytic syncytium, but K^+ must first enter
590 astrocytes through Kir4.1 channels before it can be redistributed through the network. With
591 Kir4.1 conductance reduced by 12% in VH astrocytes, the membrane represents a
592 bottleneck that limits K^+ uptake regardless of how extensive the downstream network may
593 be. Thus, gap junction coupling appears to represent a partial compensatory adaptation—
594 expanding the potential redistribution capacity—but this adaptation cannot fully overcome
595 the primary deficit in membrane conductance.

596 This interpretation suggests that Kir4.1 channel function, rather than gap junction coupling,
597 is the rate-limiting step for K^+ buffering during active neuronal stimulation in VH.

598 **Circadian regulation superimposed on stable regional identity**

599 Our temporal analysis reveals that circadian phase modulates—but does not abolish—the
600 stable regional differences in K^+ buffering. Two key parameters exhibit no circadian
601 variation: (1) the time constant of K^+ decay, which remains similar between regions and
602 constant across time, and (2) Ba^{2+}-sensitive Kir4.1 current, which shows consistent regional
603 differences (lower in VH) at all timepoints despite circadian changes in Kir4.1 protein
604 expression.

605 The stability of Kir4.1 current despite dynamic protein expression points to complex post-
606 translational regulation. At ZT3, DH exhibits 41% higher Kir4.1 protein than VH; by ZT8, this
607 regional difference disappears due to reduced expression in DH and increased expression
608 in VH. Yet functional Kir4.1 currents remain regionally differentiated throughout the day. This
609 dissociation suggests that Kir4.1 channel activity is regulated not only by protein abundance
610 but also by trafficking to the membrane, phosphorylation state, interaction with scaffolding
611 proteins, or lipid microenvironment—mechanisms that may themselves be under circadian
612 control and differ between regions.

613 The most pronounced circadian effect is observed in the convergence of multiple
614 parameters at ZT3 versus later timepoints. At early light phase, the regional divergence
615 between DH and VH is maximal: K^+ peak amplitude differs 2.1-fold, gap junction coupling
616 differs by 35%, and Kir4.1 protein expression differs by 41%. By ZT8 and ZT15, these
617 differences attenuate or reverse. This temporal pattern suggests that early light phase—
618 corresponding to the rest period in nocturnal rodents—may be a time when regional
619 specialization is most important, possibly reflecting distinct roles for dorsal and ventral

hippocampus in sleep-dependent memory consolidation, sharp-wave ripple generation, or metabolic recovery (Pronier et al., 2023).

Functional implications: regional K^+ dynamics shape circuit computations

The distinct K^+ buffering properties of DH and VH astrocytes have important implications for how these regions process information and contribute to hippocampal function. Extracellular K^+ accumulation exerts multiple effects on neuronal excitability, synaptic transmission, and network oscillations, making astrocytic control of $[K^+]_o$ a powerful regulator of circuit dynamics.

Ventral hippocampus: permissive K^+ accumulation enables synchronized network events but imposes low-pass filtering. The rapid and pronounced $[K^+]_o$ accumulation in VH has both facilitatory and inhibitory consequences. Elevated $[K^+]_o$ depolarizes neurons toward action potential threshold, enhancing NMDA receptor activation by relieving Mg^{2+} block and increasing the spatial range of glutamate spillover (Shih et al., 2013). These effects promote network synchronization and may facilitate the generation of hippocampal sharp-wave ripples (SWRs)—brief, high-frequency oscillations essential for memory consolidation. Indeed, VH slices more readily generate spontaneous SWRs than DH slices (Schlingloff et al., 2014), and CA3 pyramidal neurons in VH possess stronger recurrent connectivity and higher intrinsic excitability (Sun et al., 2020), properties that synergize with permissive K^+ accumulation to support synchronized discharges.

However, sustained K^+ elevation during prolonged activity also inactivates voltage-gated Na^+ channels and reduces the driving force for K^+ efflux through voltage-gated K^+ channels,

641 leading to synaptic depression and reduced responsiveness to repetitive stimulation (Meeks
642 & Mennerick, 2004). This creates a functional low-pass filter, where VH responds robustly to
643 initial or low-frequency inputs but saturates during sustained high-frequency activity. Such
644 filtering may prevent runaway excitation and protect against seizure propagation, while
645 simultaneously biasing VH toward processing sparse, salient events rather than sustained
646 information streams.

647 Dorsal hippocampus: tight K^+ control preserves high-fidelity transmission and supports
648 frequency-dependent facilitation. In contrast to VH, the strong Kir4.1-mediated buffering in
649 DH maintains lower $[K^+]_o$ during neuronal activity, preserving neuronal excitability and
650 enabling synaptic facilitation at frequencies between 10-50 Hz—precisely the range that
651 encodes behaviorally relevant information (Papaleonidopoulos et al., 2017). Lower K^+
652 accumulation prevents synaptic depression, supporting sustained information transfer and
653 communication with neocortical targets (Moreno et al., 2016). This configuration suits DH
654 for high-pass filtering: reliable transmission of sustained, structured activity patterns
655 required for spatial navigation, episodic memory encoding, and cognitive map formation
656 (Fanselow & Dong, 2010).

657 The metabolic consequences of these regional differences are consistent with recent
658 findings that VH relies more heavily on aerobic glycolysis—generating cytosolic ATP rapidly
659 but inefficiently—compared to the oxidative phosphorylation favored in DH (Brancati et al.,
660 2021). The elevated Na^+/K^+-ATPase activity required to clear excess K^+ in VH imposes
661 substantial energetic demands that may be preferentially met by glycolytic metabolism.

662 **Pathological implications: regional K^+ dysregulation and epilepsy**

663 The reduced K^+ buffering capacity of VH astrocytes provides a mechanistic framework for
664 understanding the well-established vulnerability of VH to seizures. Evidence from human
665 temporal lobe epilepsy (TLE) and animal models identifies VH as the primary seizure
666 initiation zone (Babb et al., 1984; Bernasconi et al., 2003; Buckmaster et al., 2022; Toyoda
667 et al., 2013). Our findings suggest that intrinsic differences in astrocytic K^+ buffering—
668 present even in healthy tissue—predispose VH to hyperexcitability.

669 During pathological conditions such as epilepsy, when neuronal activity is abnormally
670 intense and synchronized, the limited Kir4.1 capacity in VH would result in excessive $[K^+]_o$
671 accumulation, reaching levels (>10 mM) known to be associated with or even trigger
672 seizures (de Curtis et al., 2018; Enger et al., 2015). Furthermore, epileptic tissue exhibits
673 downregulation of Kir4.1 expression and function (Bataveljic et al., 2024; Romanos et al.,
674 2020), exacerbating the baseline deficit in VH and creating a positive feedback loop, i.e.
675 reduced buffering results in greater K^+ accumulation, which enhances excitability and thus
676 more intense neuronal firing, favoring further K^+ release.

677 The circadian modulation of K^+ buffering we observe also provides a potential mechanism
678 for the circadian rhythmicity of seizure occurrence documented in epilepsy patients and
679 animal models (B.-L. Chang et al., 2018; Proix et al., 2021; Quigg et al., 2000). Seizure
680 susceptibility peaks during specific circadian phases, and our data suggest that times of
681 maximal regional divergence in K^+ buffering (e.g., ZT3) may correspond to windows of
682 heightened vulnerability in VH. Conversely, circadian phases when regional differences

683 attenuate may represent periods of reduced seizure risk. However, given the extensive
684 reorganization of circuits in epilepsy, it will be important to assess all the above-described
685 properties in experimental epilepsy.

686 **Dissociation between Kir4.1 protein expression and functional current: post-**
687 **translational complexity**

688 One of the most intriguing findings is the dissociation between Kir4.1 protein expression
689 dynamics (which vary significantly across circadian time) and functional Kir4.1-mediated
690 currents (which show stable regional differences but no temporal variation). This
691 dissociation implies that channel function is regulated at multiple levels beyond simple
692 protein abundance.

693 Several post-translational mechanisms could account for this complexity. Kir4.1 channels
694 must traffic to the plasma membrane to be functional, and this trafficking is regulated by
695 interactions with scaffolding proteins such as dystrophin-associated protein complex and
696 α-syntrophin (reviewed in (Olsen & Sontheimer, 2008)). Circadian changes in trafficking
697 machinery or cytoskeletal organization could alter the proportion of synthesized channels
698 that reach the membrane. Additionally, Kir4.1 activity is modulated by phosphorylation, pH,
699 and membrane lipid composition (Hibino et al., 2010)—all of which exhibit circadian
700 oscillations (McCauley et al., 2020; Ryu et al., 2024). Finally, Kir4.1 channels interact with
701 other membrane proteins in macromolecular complexes, and changes in these interactions
702 could alter channel open probability or conductance without changing total protein levels.

703 The persistence of regional differences in functional current despite convergence of protein
704 expression also suggests that DH and VH astrocytes may differ in their complement of
705 regulatory proteins or post-translational modifications. Identifying these region-specific
706 regulatory mechanisms represents an important direction for future research and could
707 reveal novel targets for modulating astrocytic K^+ buffering in disease states.

708 **Comparative context: astrocytic heterogeneity as a general principle**

709 Our findings contribute to a growing recognition that astrocytic heterogeneity is a
710 fundamental organizational principle across the brain. Astrocytes differ between brain
711 regions in molecular marker expression, morphology, calcium signaling dynamics,
712 glutamate uptake capacity, and contribution to synaptic function (reviewed in (Khakh &
713 Deneen, 2019)). Within the hippocampus, dorsoventral differences in astrocytic gene
714 expression, morphology, and calcium dynamics have been documented (Dong et al., 2009;
715 Jinno, 2011; Ryu et al., 2024; Thompson et al., 2008), but the functional consequences of
716 this heterogeneity for circuit physiology have remained unclear.

717 Our demonstration that astrocytic K^+ buffering—a core homeostatic function—exhibits
718 pronounced regional and temporal variation establishes that astrocytic heterogeneity is not
719 merely a descriptive phenomenon but has direct, measurable impacts on network
720 excitability and information processing. This principle likely extends beyond the
721 hippocampus to other brain structures where astrocytic properties may be tuned to local
722 circuit demands.

723 Importantly, our findings challenge the traditional view of astrocytes as passive, uniform
724 support cells that maintain brain homeostasis in a spatially and temporally invariant
725 manner. Instead, astrocytes emerge as active, heterogeneous participants in circuit
726 function whose properties are dynamically regulated in space and time. This has
727 implications for understanding both normal brain function and the pathophysiology of
728 neurological disorders.

729 **Reconciling slice physiology with in vivo function: caveats and considerations**

730 Several important caveats limit the interpretation of our findings. First, our measurements
731 were performed in acute brain slices, which lack the intact vascular system, interstitial fluid
732 flow, and long-range connectivity present in vivo. K^+ clearance mechanisms that rely on
733 vascular uptake or long-distance redistribution through white matter tracts may be
734 compromised in slices, potentially altering the relative contributions of different buffering
735 mechanisms. Evidence suggests that gap junction-mediated spatial buffering contributes
736 more to K^+ clearance in vivo than in slices, raising the possibility that the enhanced gap
737 junction coupling we observe in VH may be more functionally significant in intact brain than
738 our slice experiments suggest (Breithausen et al., 2020; Cooper et al., 2025).

739 Second, patch-clamp approach in astrocytes samples a small radius of somata (Zhou et al.,
740 2021), which may not fully represent the properties of fine perisynaptic processes where K^+
741 buffering most directly impacts synaptic function. Recent advances in voltage imaging
742 reveal that distal astrocytic processes experience larger depolarizations in response to
743 neuronal activity than somata do (Armbruster et al., 2022), and spatial

744 compartmentalization of ion channels may create local K^+ buffering microdomains that our
745 somatic recordings cannot detect. Additionally, we used GFAP immunolabeling to define
746 astrocytic regions for Kir4.1 quantification, but GFAP labels only ~15% of astrocyte volume
747 (Bushong et al., 2002), biasing our analysis toward the most GFAP-rich cellular
748 compartments and underestimating Kir4.1 in fine processes.

749 Third, our sampling of three circadian timepoints (ZT3, ZT8, ZT15) provides valuable initial
750 insight into temporal regulation but may miss peak effects occurring at other phases. Higher
751 temporal resolution studies examining more timepoints throughout the 24-hour cycle would
752 provide a more complete picture of circadian dynamics.

753 Despite these limitations, our findings reveal fundamental principles of astrocytic K^+
754 regulation that likely persist—and may be amplified—in vivo. The regional differences we
755 document are substantial (2-fold differences in K^+ peak amplitude, 41% difference in Kir4.1
756 current) and consistent across multiple experimental approaches, suggesting they reflect
757 robust biological properties rather than experimental artifacts.

758 **Future directions and therapeutic implications**

759 Our findings open several important avenues for future investigation. First, determining the
760 molecular mechanisms underlying circadian regulation of Kir4.1 function—including
761 identification of post-translational modifications, trafficking pathways, and regulatory
762 proteins that differ between DH and VH—could reveal novel targets for modulating
763 astrocytic K^+ buffering. Second, extending these studies to in vivo preparations using
764 genetically encoded K^+ sensors and astrocyte-specific manipulations would clarify how the

765 slice-based findings translate to intact circuits and behavior. Third, investigating whether
766 similar regional and temporal heterogeneity exists in human hippocampus and whether
767 these properties are altered in epilepsy could open the way to novel therapeutic avenues.

768 From a therapeutic perspective, our findings suggest that strategies to enhance astrocytic
769 K^+ buffering might need to be both regionally and temporally targeted. Global upregulation
770 of Kir4.1 expression throughout the brain could have unintended consequences in regions
771 where current expression levels are functionally appropriate. Similarly, chronotherapeutic
772 approaches that time interventions to periods of maximum vulnerability—when regional
773 differences in buffering capacity are most pronounced—may prove more effective than
774 continuous treatment.

775 Gene therapy approaches to selectively enhance Kir4.1 expression in VH astrocytes
776 represent a particularly promising avenue. Adeno-associated viral vectors with astrocyte-
777 specific promoters (Tyurikova et al., 2025) could deliver Kir4.1 cDNA to VH, potentially
778 normalizing its K^+ buffering capacity to DH-like levels and reducing seizure susceptibility.
779 Alternatively, small molecules that enhance Kir4.1 channel open probability or trafficking to
780 the membrane could achieve similar therapeutic effects through pharmacological means.

781 **Conclusion**

782 This study establishes that astrocytic K^+ buffering in the hippocampus is neither spatially
783 uniform nor temporally static but instead exhibits regional and circadian heterogeneity.
784 Ventral hippocampal astrocytes possess intrinsically reduced Kir4.1-mediated K^+
785 conductance, resulting in rapid K^+ accumulation during neuronal activity that is partially

786 compensated by putative enhanced Na^+/K^+-ATPase activity and expanded gap junction
787 coupling. These regional specializations do not simply mirror neuronal excitability patterns
788 but may actively shape them, creating distinct computational regimes in dorsal versus
789 ventral hippocampus. Superimposed on this stable regional identity is a circadian layer of
790 regulation that modulates—but does not abolish—regional differences, with maximal
791 divergence during early light phase.

792 Our findings support the view that astrocytes as active, heterogeneous participants in circuit
793 function whose homeostatic properties are dynamically tuned in space and time. This has
794 implications extending beyond the hippocampus to other brain regions and beyond K^+
795 buffering to other astrocytic functions. By revealing how regional and temporal factors
796 converge to determine astrocytic K^+ regulation, this work provides a mechanistic framework
797 for understanding hippocampal circuit dynamics in health and offers potentially new
798 therapeutic strategies for epilepsy based on targeted modulation of astrocytic function at
799 specific times and locations.

800

801 **Figure Captions**

802 **Figure 1. Network level extracellular K+ recording**

803 **A**) Example of anatomical structures of dorsal (DH: red) and ventral (VH: blue) hippocampal
804 slices.

805 **B**) Schematic arrangement of stimulation of Schaffer Collateral (SC), recording of local field
806 potential (LFP) from the *stratum oriens* (*s.o.*), and K+ recording $[K^+]_o$ from *stratum radiatum*
807 (*s.r.*). Example trace of $[K^+]_o$ in DH (red) and VH (blue) in response to 10Hz30s stimulation.

808 **C**-**G**) Normalized LFP integral, 25-75% rise time, peak amplitude, tau decay of
809 monoexponentially fitted, and undershoot amplitude across DH and VH in three ZT3, ZT8,
810 and ZT15

811 Analyses, based on a lognormal distribution model, are reported as posterior median
812 estimates with 95% credible intervals.

813 * $P < 0.05$, ** $P < 0.01$. Statistical significance was calculated using two-sided unpaired
814 Mann–Whitney U test.

815 [DH_ZT3: n =16 (N = 8) , DH_ZT8: n =16 (N= 8), DH_ZT5: n =19 (N = 10), VH_ZT3: n =16 (N=8),
816 VH_ZT8: n =18 (N= 9), VH_ZT5: n =19 (N=10)]

817 **Figure 2. Gap junction coupling across hippocampal regions and time of day**

818 **A**) Inverted example image of the coupled astrocytes in a hippocampal slice, as obtained
819 after biocytin diffusion from a single cell, held in whole-cell voltage clamp for 20 mins. Scale
820 bar is equal to 50 μm.

821 **B**) Summary of the number of biocytin-coupled cell across DH and VH in different time
822 points (ZT3, 8, 15). Analyses, based on a lognormal distribution model, are reported as
823 posterior median estimates with 95% credible intervals. *$p < 0.05$ Mann–Whitney U test;
824 *s.p., Stratum pyramidale*; *s.r., stratum radiatum*.

825 [DH_ZT3: n =11 (N = 6) , DH_ZT8: n =15 (N= 6), DH_ZT5: n =11 (N = 6), VH_ZT3: n =12 (N=7),
826 VH_ZT8: n =11 (N= 7), VH_ZT5: n =9 (N=6)]

827 **Figure 3. Regional differences across regions and time**

828 **A**) Wide-field image of stained astrocytes with SR101.

829 **B**) Left: example image of biocytin stained astrocytes in absence of MFA versus incubated in
830 MFA (right). *S.r., stratum radiatum; s.l.m., stratum lacunosum moleculare*. Scale bar is
831 equal to 20 µm.

832 **C**) statistical summary of the coupled cell number in both groups. Addition of MFA results in
833 an average reduction of -86 [95%CI -95, -72], $p < .00001$.

834 **D**) Initial resting membrane potential (RMP; in mV) of the patched astrocytes across DH and
835 VH in ZT3, ZT8, and ZT15.

836 **E**) Ba^{2+}-induced depolarization across the regions and time. No significant effect of region
837 and time was observed, except in an isolated incident of ZT8.

838 **F**) Ba^{2+}-sensitive current obtained by subtracting membrane currents elicited in whole-cell
839 configuration (from -140 mV to +50 mV, 10 mV increment; holding potential = −70 mV) from
840 the baseline: DH (red) and VH (blue). The rectification of measurements are based on the

841 barium-sensitive currents. The IV curve slope of -140 to -100mV interval (green) was divided
842 to the slope of 10mV to 50mV (magenta), and rectification profile of the tested cell was
843 determined given the ratios.

844 **G**)) Kir4.1 current across the regions and time of day. Significant main effect of region was
845 observed without the influence of time.

846 Analyses are reported as posterior median estimates with 95% credible intervals.

847 **H**) Proportion of rectifying astrocytes (blue) versus non-rectifying (orange) across DH and
848 VH.

849 [DH_ZT3: n = 9 (N = 7) , DH_ZT8: n = 5 (N= 3), DH_ZT5: n =8 (N = 6), VH_ZT3: n =9 (N=6),
850 VH_ZT8: n =8 (N= 5), VH_ZT5: n =10 (N=5)]

851 * $P < 0.05$, ***$P < 0.001$. Statistical significance was calculated using two-sided unpaired
852 Mann–Whitney U test

853 **Figure 4. Regional differences in Kir4.1 expression along the dorsoventral axis depends**
854 **on time**

855 **A**) Representative examples of confocal images of immunofluorescent labeling of Kir4.1
856 (red) and astrocyte marker glial fibrillary acidic protein (GFAP, green) , and DAPI (blue) for
857 DH (Left) and VH (Right), at 20x magnification (scale bar = 100 μm).

858 **B**) Higher magnification of confocal images of Kir4.1 (red) and astrocyte marker glial fibrillary
859 acidic protein (GFAP, green), and the merging of the two. Images were taken from the s.r.

C) Fraction of GFAP positive area with Kir4.1 protein is significantly smaller in DH -1.72% [95%CI -2.6%, -0.88%], and this effect is driven by ZT8 -2.21% [95%CI -3.12%, -1.11%].

D) Quantification of Kir4.1 integrated density normalized to GFAP. The relationship was only significant in ZT3, where VH showed -46% (less) than DH [95%CI -74%, -19%].

Analyses, based on a student t-distribution model, are reported as posterior median estimates with 95% credible intervals.

* $P < 0.05$. Statistical significance was calculated using two-sided unpaired Mann–Whitney U test

[DH_ZT3: n = 11 (N = 1) , DH_ZT8: n = 16 (N= 1), DH_ZT5: n =9 (N = 1), VH_ZT3: n =12 (N=1), VH_ZT8: n =15 (N= 1), VH_ZT5: n =11 (N=1)]

Figure 5. Graphical summary of the results

References

Anderson, T. R., Huguenard, J. R., & Prince, D. A. (2010). Differential effects of Na+–K+ ATPase blockade on cortical layer V neurons. *The Journal of Physiology*, *588*(22), 4401–4414. https://doi.org/10.1113/jphysiol.2010.191858

Anderson, U. A., Carson, C., & McCloskey, K. D. (2009). KCNQ currents and their contribution to resting membrane potential and the excitability of interstitial cells of Cajal from the guinea pig bladder. *The Journal of Urology*, *182*(1), 330–336. https://doi.org/10.1016/j.juro.2009.02.108

Armbruster, M., Naskar, S., Garcia, J. P., Sommer, M., Kim, E., Adam, Y., Haydon, P. G., Boyden, E. S., Cohen, A. E., & Dulla, C. G. (2022). Neuronal activity drives pathway-specific depolarization of peripheral astrocyte processes. *Nature Neuroscience*, *25*(5), Article 5. https://doi.org/10.1038/s41593-022-01049-x

Babb, T. L., Brown, W. J., Pretorius, J., Davenport, C., Lieb, J. P., & Crandall, P. H. (1984). Temporal Lobe Volumetric Cell Densities in Temporal Lobe Epilepsy. *Epilepsia*, *25*(6), 729–740. https://doi.org/10.1111/j.1528-1157.1984.tb03484.x

Bataveljic, D., Pivonkova, H., de Concini, V., Hébert, B., Ezan, P., Briault, S., Bemelmans, A.-P., Pichon, J., Menuet, A., & Rouach, N. (2024). Astroglial Kir4.1 potassium channel deficit drives neuronal hyperexcitability and behavioral defects in Fragile X syndrome mouse model. *Nature Communications*, *15*, 3583. https://doi.org/10.1038/s41467-024-47681-y

Bernasconi, N., Bernasconi, A., Caramanos, Z., Antel, S. B., Andermann, F., & Arnold, D. L. (2003). Mesial temporal damage in temporal lobe epilepsy: A volumetric MRI study

of the hippocampus, amygdala and parahippocampal region. *Brain*, *126*(2), 462–469. https://doi.org/10.1093/brain/awg034

Brancati, G. E., Rawas, C., Ghestem, A., Bernard, C., & Ivanov, A. I. (2021). Spatio-temporal heterogeneity in hippocampal metabolism in control and epilepsy conditions. *Proceedings of the National Academy of Sciences*, *118*(11), e2013972118. https://doi.org/10.1073/pnas.2013972118

Breithausen, B., Kautzmann, S., Boehlen, A., Steinhäuser, C., & Henneberger, C. (2020). Limited contribution of astroglial gap junction coupling to buffering of extracellular K^+ in CA1 stratum radiatum. *Glia*, *68*(5), 918–931. https://doi.org/10.1002/glia.23751

Buckmaster, P. S., Reyes, B., Kahn, T., & Wyeth, M. (2022). Ventral Hippocampal Formation Is the Primary Epileptogenic Zone in a Rat Model of Temporal Lobe Epilepsy. *Journal of Neuroscience*, *42*(39), 7482–7495. https://doi.org/10.1523/JNEUROSCI.0429-22.2022

Bürkner, P.-C. (2017). brms: An R Package for Bayesian Multilevel Models Using Stan. *Journal of Statistical Software*, *80*, 1–28. https://doi.org/10.18637/jss.v080.i01

Bushong, E. A., Martone, M. E., Jones, Y. Z., & Ellisman, M. H. (2002). Protoplasmic Astrocytes in CA1 Stratum Radiatum Occupy Separate Anatomical Domains. *The Journal of Neuroscience*, *22*(1), 183–192. https://doi.org/10.1523/JNEUROSCI.22-01-00183.2002

Chang, B.-L., Leite, M., Snowball, A., Lieb, A., Chabrol, E., Walker, M. C., Kullmann, D. M., Schorge, S., & Wykes, R. C. (2018). Semiology, clustering, periodicity and natural

915 history of seizures in an experimental occipital cortical epilepsy model. *Disease*
916 *Models & Mechanisms*, *11*(12), dmm036194. https://doi.org/10.1242/dmm.036194
917 Chang, W.-C., Kudlacek, J., Hlinka, J., Chvojka, J., Hadrava, M., Kumpost, V., Powell, A. D.,
918 Janca, R., Maturana, M. I., Karoly, P. J., Freestone, D. R., Cook, M. J., Palus, M.,
919 Otahal, J., Jefferys, J. G. R., & Jiruska, P. (2018). Loss of neuronal network resilience
920 precedes seizures and determines the ictogenic nature of interictal synaptic
921 perturbations. *Nature Neuroscience*, *21*(12), 1742–1752.
922 https://doi.org/10.1038/s41593-018-0278-y
923 Chever, O., Djukic, B., McCarthy, K. D., & Amzica, F. (2010). Implication of Kir4.1 Channel
924 in Excess Potassium Clearance: An In Vivo Study on Anesthetized Glial-Conditional
925 Kir4.1 Knock-Out Mice. *Journal of Neuroscience*, *30*(47), 15769–15777.
926 https://doi.org/10.1523/JNEUROSCI.2078-10.2010
927 Cooper, M. L., Selles, M. C., Cammer, M., Gildea, H. K., Sall, J., Chiurri, K. E., Saab, A. S.,
928 Liddelow, S. A., & Chao, M. V. (2025). Astrocytes connect specific brain regions
929 through plastic gap junctional networks. *bioRxiv: The Preprint Server for Biology*,
930 2025.07.18.665573. https://doi.org/10.1101/2025.07.18.665573
931 D'Ambrosio, R., Gordon, D. S., & Winn, H. R. (2002). Differential role of KIR channel and
932 Na(+)/K(+)-pump in the regulation of extracellular K(+) in rat hippocampus. *Journal*
933 *of Neurophysiology*, *87*(1), 87–102. https://doi.org/10.1152/jn.00240.2001
934 de Curtis, M., Uva, L., Gnatkovsky, V., & Librizzi, L. (2018). Potassium dynamics and
935 seizures: Why is potassium ictogenic? *Epilepsy Research*, *143*, 50–59.
936 https://doi.org/10.1016/j.eplepsyres.2018.04.005

Debski, K. J., Ceglia, N., Ghestem, A., Ivanov, A. I., Brancati, G. E., Bröer, S., Bot, A. M., Müller, J. A., Schoch, S., Becker, A., Löscher, W., Guye, M., Sassone-Corsi, P., Lukasiuk, K., Baldi, P., & Bernard, C. (2020). The circadian dynamics of the hippocampal transcriptome and proteome is altered in experimental temporal lobe epilepsy. *Science Advances*, *6*(41), eaat5979. https://doi.org/10.1126/sciadv.aat5979

Delignette-Muller, M. L., & Dutang, C. (2015). fitdistrplus: An R Package for Fitting Distributions. *Journal of Statistical Software*, *64*, 1–34. https://doi.org/10.18637/jss.v064.i04

Djukic, B., Casper, K. B., Philpot, B. D., Chin, L.-S., & McCarthy, K. D. (2007). Conditional Knock-Out of K_{ir} 4.1 Leads to Glial Membrane Depolarization, Inhibition of Potassium and Glutamate Uptake, and Enhanced Short-Term Synaptic Potentiation. *The Journal of Neuroscience*, *27*(42), 11354–11365. https://doi.org/10.1523/JNEUROSCI.0723-07.2007

Dong, H.-W., Swanson, L. W., Chen, L., Fanselow, M. S., & Toga, A. W. (2009). Genomic–anatomic evidence for distinct functional domains in hippocampal field CA1. *Proceedings of the National Academy of Sciences*, *106*(28), 11794–11799. https://doi.org/10.1073/pnas.0812608106

Dospinescu, V.-M., Mascarenhas, A., Butler, J., Nijjar, S., Taborda, K. de O., Connors, S., Huang, L., & Dale, N. (2025). CO2-dependent opening of Connexin 43 hemichannels. *eLife*, *14*. https://doi.org/10.7554/eLife.105989.2

Dougherty, K. A., Islam, T., & Johnston, D. (2012). Intrinsic excitability of CA1 pyramidal neurones from the rat dorsal and ventral hippocampus. *The Journal of Physiology*, *590*(Pt 22), 5707–5722. https://doi.org/10.1113/jphysiol.2012.242693

Enger, R., Tang, W., Vindedal, G. F., Jensen, V., Johannes Helm, P., Sprengel, R., Looger, L. L., & Nagelhus, E. A. (2015). Dynamics of Ionic Shifts in Cortical Spreading Depression. *Cerebral Cortex (New York, NY)*, *25*(11), 4469–4476. https://doi.org/10.1093/cercor/bhv054

Erecińska, M., & Silver, I. A. (1994). Ions and energy in mammalian brain. *Progress in Neurobiology*, *43*(1), 37–71. https://doi.org/10.1016/0301-0082(94)90015-9

Fanselow, M. S., & Dong, H.-W. (2010). Are the Dorsal and Ventral Hippocampus Functionally Distinct Structures? *Neuron*, *65*(1), 7–19. https://doi.org/10.1016/j.neuron.2009.11.031

Heinemann, U., & Arens, J. (1992). Production and calibration of ion-sensitive microelectrodes. *Practical Electrophysiological Methods*, 206–212.

Hibino, H., Inanobe, A., Furutani, K., Murakami, S., Findlay, I., & Kurachi, Y. (2010). Inwardly rectifying potassium channels: Their structure, function, and physiological roles. *Physiological Reviews*, *90*(1), 291–366. https://doi.org/10.1152/physrev.00021.2009

Ho, J., Tumkaya, T., Aryal, S., Choi, H., & Claridge-Chang, A. (2019). Moving beyond P values: Data analysis with estimation graphics. *Nature Methods*, *16*(7), 565–566. https://doi.org/10.1038/s41592-019-0470-3

Jinno, S. (2011). Regional and laminar differences in antigen profiles and spatial distributions of astrocytes in the mouse hippocampus, with reference to aging. *Neuroscience*, *180*, 41–52. https://doi.org/10.1016/j.neuroscience.2011.02.013

Khakh, B. S., & Deneen, B. (2019). The Emerging Nature of Astrocyte Diversity. *Annual Review of Neuroscience*, *42*, 187–207. https://doi.org/10.1146/annurev-neuro-070918-050443

Kherad-Pajouh, S., & Renaud, O. (2015). A general permutation approach for analyzing repeated measures ANOVA and mixed-model designs. *Statistical Papers*, *56*(4), 947–967. https://doi.org/10.1007/s00362-014-0617-3

Larsen, B. R., Assentoft, M., Cotrina, M. L., Hua, S. Z., Nedergaard, M., Kaila, K., Voipio, J., & MacAulay, N. (2014). Contributions of the Na^+/K^+-ATPase, NKCC1, and Kir4.1 to hippocampal K^+ clearance and volume responses: Mechanisms of K^+ Clearance in the Brain. *Glia*, *62*(4), 608–622. https://doi.org/10.1002/glia.22629

Larsen, B. R., & MacAulay, N. (2014). Kir4.1-mediated spatial buffering of K+: Experimental challenges in determination of its temporal and quantitative contribution to K+ clearance in the brain. *Channels*, *8*(6), 544–550. https://doi.org/10.4161/19336950.2014.970448

Lu, W., & Haber, S. N. (1992). In situ hybridization histochemistry: A new method for processing material stored for several years. *Brain Research*, *578*(1), 155–160. https://doi.org/10.1016/0006-8993(92)90243-3

MacAulay, N. (2020). Molecular mechanisms of K+ clearance and extracellular space shrinkage—Glia cells as the stars. *Glia*, *68*(11), 2192–2211. https://doi.org/10.1002/glia.23824

McCauley, J. P., Petroccione, M. A., D'Brant, L. Y., Todd, G. C., Affinnih, N., Wisnoski, J. J., Zahid, S., Shree, S., Sousa, A. A., De Guzman, R. M., Migliore, R., Brazhe, A., Leapman, R. D., Khmaladze, A., Semyanov, A., Zuloaga, D. G., Migliore, M., & Scimemi, A. (2020). Circadian Modulation of Neurons and Astrocytes Controls Synaptic Plasticity in Hippocampal Area CA1. *Cell Reports*, *33*(2), 108255. https://doi.org/10.1016/j.celrep.2020.108255

Meeks, J. P., & Mennerick, S. (2004). Selective Effects of Potassium Elevations on Glutamate Signaling and Action Potential Conduction in Hippocampus. *The Journal of Neuroscience*, *24*(1), 197–206. https://doi.org/10.1523/JNEUROSCI.4845-03.2004

Moreno, A., Morris, R. G. M., & Canals, S. (2016). Frequency-Dependent Gating of Hippocampal-Neocortical Interactions. *Cerebral Cortex (New York, N.Y.: 1991)*, *26*(5), 2105–2114. https://doi.org/10.1093/cercor/bhv033

Nimmerjahn, A., Kirchhoff, F., Kerr, J. N. D., & Helmchen, F. (2004). Sulforhodamine 101 as a specific marker of astroglia in the neocortex in vivo. *Nature Methods*, *1*(1), 31–37. https://doi.org/10.1038/nmeth706

Olsen, M. L., & Sontheimer, H. (2008). Functional implications for Kir4.1 channels in glial biology: From K+ buffering to cell differentiation. *Journal of Neurochemistry*, *107*(3), 589–601. https://doi.org/10.1111/j.1471-4159.2008.05615.x

Papaleonidopoulos, V., Trompoukis, G., Koutsoumpa, A., & Papatheodoropoulos, C. (2017). A gradient of frequency-dependent synaptic properties along the longitudinal hippocampal axis. *BMC Neuroscience*, *18*, 79. https://doi.org/10.1186/s12868-017-0398-4

Papatheodoropoulos, C., Moschovos, C., & Kostopoulos, G. (2005). Greater contribution of N-methyl-d-aspartic acid receptors in ventral compared to dorsal hippocampal slices in the expression and long-term maintenance of epileptiform activity. *Neuroscience*, *135*(3), 765–779. https://doi.org/10.1016/j.neuroscience.2005.06.024

Peretz, A., Degani, N., Nachman, R., Uziyel, Y., Gibor, G., Shabat, D., & Attali, B. (2005). Meclofenamic Acid and Diclofenac, Novel Templates of KCNQ2/Q3 Potassium Channel Openers, Depress Cortical Neuron Activity and Exhibit Anticonvulsant Properties. *Molecular Pharmacology*, *67*(4), 1053–1066. https://doi.org/10.1124/mol.104.007112

Proix, T., Truccolo, W., Leguia, M. G., Tcheng, T. K., King-Stephens, D., Rao, V. R., & Baud, M. O. (2021). Forecasting seizure risk in adults with focal epilepsy: A development and validation study. *The Lancet Neurology*, *20*(2), 127–135. https://doi.org/10.1016/S1474-4422(20)30396-3

Pronier, É., Morici, J. F., & Girardeau, G. (2023). The role of the hippocampus in the consolidation of emotional memories during sleep. *Trends in Neurosciences*, *46*(11), 912–925. https://doi.org/10.1016/j.tins.2023.08.003

Quigg, M., Clayburn, H., Straume, M., Menaker, M., & Bertram III, E. H. (2000). Effects of Circadian Regulation and Rest—Activity State on Spontaneous Seizures in a Rat Model of Limbic Epilepsy. *Epilepsia*, *41*(5), 502–509. https://doi.org/10.1111/j.1528-1157.2000.tb00202.x

Romanos, J., Benke, D., Pietrobon, D., Zeilhofer, H. U., & Santello, M. (2020). Astrocyte dysfunction increases cortical dendritic excitability and promotes cranial pain in familial migraine. *Science Advances*, *6*(23), eaaz1584. https://doi.org/10.1126/sciadv.aaz1584

Ryu, J. E., Shim, K.-W., Roh, H. W., Park, M., Lee, J.-H., & Kim, E. Y. (2024). Circadian regulation of endoplasmic reticulum calcium response in mouse cultured astrocytes. *eLife*, *13*. https://doi.org/10.7554/eLife.96357.1

Schlingloff, D., Káli, S., Freund, T. F., Hájos, N., & Gulyás, A. I. (2014). Mechanisms of Sharp Wave Initiation and Ripple Generation. *The Journal of Neuroscience*, *34*(34), 11385–11398. https://doi.org/10.1523/JNEUROSCI.0867-14.2014

Seifert, G., Huttmann, K., Binder, D. K., Hartmann, C., Wyczynski, A., Neusch, C., & Steinhauser, C. (2009). Analysis of Astroglial K+ Channel Expression in the Developing Hippocampus Reveals a Predominant Role of the Kir4.1 Subunit. *Journal of Neuroscience*, *29*(23), 7474–7488. https://doi.org/10.1523/JNEUROSCI.3790-08.2009

Shih, P.-Y., Savtchenko, L. P., Kamasawa, N., Dembitskaya, Y., McHugh, T. J., Rusakov, D. A., Shigemoto, R., & Semyanov, A. (2013). Retrograde Synaptic Signaling Mediated

by K+ Efflux through Postsynaptic NMDA Receptors. *Cell Reports*, *5*(4), 941–951. https://doi.org/10.1016/j.celrep.2013.10.026

Stephan, J., Eitelmann, S., & Zhou, M. (2021). Approaches to Study Gap Junctional Coupling. *Frontiers in Cellular Neuroscience*, *15*, 640406. https://doi.org/10.3389/fncel.2021.640406

Sun, Q., Jiang, Y.-Q., & Lu, M. C. (2020). Topographic heterogeneity of intrinsic excitability in mouse hippocampal CA3 pyramidal neurons. *Journal of Neurophysiology*, *124*(4), 1270–1284. https://doi.org/10.1152/jn.00147.2020

Thompson, C. L., Pathak, S. D., Jeromin, A., Ng, L. L., MacPherson, C. R., Mortrud, M. T., Cusick, A., Riley, Z. L., Sunkin, S. M., Bernard, A., Puchalski, R. B., Gage, F. H., Jones, A. R., Bajic, V. B., Hawrylycz, M. J., & Lein, E. S. (2008). Genomic anatomy of the hippocampus. *Neuron*, *60*(6), 1010–1021. https://doi.org/10.1016/j.neuron.2008.12.008

Tovar, K. R., Maher, B. J., & Westbrook, G. L. (2009). Direct Actions of Carbenoxolone on Synaptic Transmission and Neuronal Membrane Properties. *Journal of Neurophysiology*, *102*(2), 974–978. https://doi.org/10.1152/jn.00060.2009

Toyoda, I., Bower, M. R., Leyva, F., & Buckmaster, P. S. (2013). Early Activation of Ventral Hippocampus and Subiculum during Spontaneous Seizures in a Rat Model of Temporal Lobe Epilepsy. *The Journal of Neuroscience*, *33*(27), 11100–11115. https://doi.org/10.1523/JNEUROSCI.0472-13.2013

Tyurikova, O., Kopach, O., Zheng, K., Rathore, D., Codadu, N., Wu, S.-Y., Shen, Y., Campbell, R. E., Wykes, R. C., Volynski, K., Savtchenko, L. P., & Rusakov, D. A.

(2025). Astrocyte Kir4.1 expression level territorially controls excitatory transmission in the brain. *Cell Reports*, *44*(2), 115299. https://doi.org/10.1016/j.celrep.2025.115299

Wallraff, A., Köhling, R., Heinemann, U., Theis, M., Willecke, K., & Steinhäuser, C. (2006). The Impact of Astrocytic Gap Junctional Coupling on Potassium Buffering in the Hippocampus. *The Journal of Neuroscience*, *26*(20), 5438–5447. https://doi.org/10.1523/JNEUROSCI.0037-06.2006

Walz, W. (2000). Role of astrocytes in the clearance of excess extracellular potassium. *Neurochemistry International*, *36*(4), 291–300. https://doi.org/10.1016/S0197-0186(99)00137-0

Wang, F., Smith, N. A., Xu, Q., Fujita, T., Baba, A., Matsuda, T., Takano, T., Bekar, L., & Nedergaard, M. (2012). Astrocytes Modulate Neural Network Activity by Ca2+-Dependent Uptake of Extracellular K+. *Science Signaling*, *5*(218), ra26. https://doi.org/10.1126/scisignal.2002334

Watson, R. E., Wiegand, S. J., Clough, R. W., & Hoffman, G. E. (1986). Use of cryoprotectant to maintain long-term peptide immunoreactivity and tissue morphology. *Peptides*, *7*(1), 155–159. https://doi.org/10.1016/0196-9781(86)90076-8

Zhou, M., Du, Y., Aten, S., & Terman, D. (2021). On the electrical passivity of astrocyte potassium conductance. *Journal of Neurophysiology*, *126*(4), 1403–1419. https://doi.org/10.1152/jn.00330.2021

1106 Figure 1

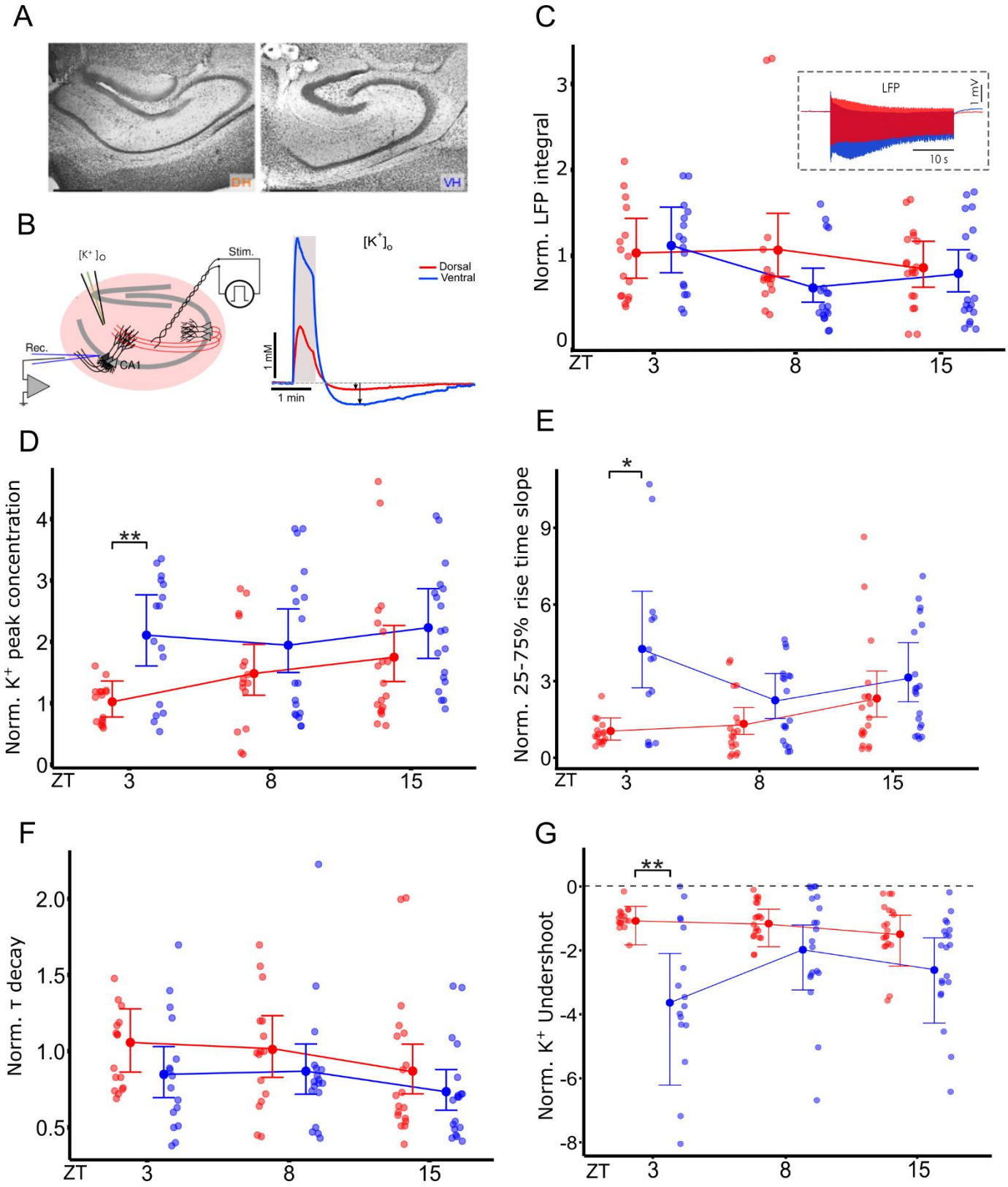

1107

1108 Figure 2

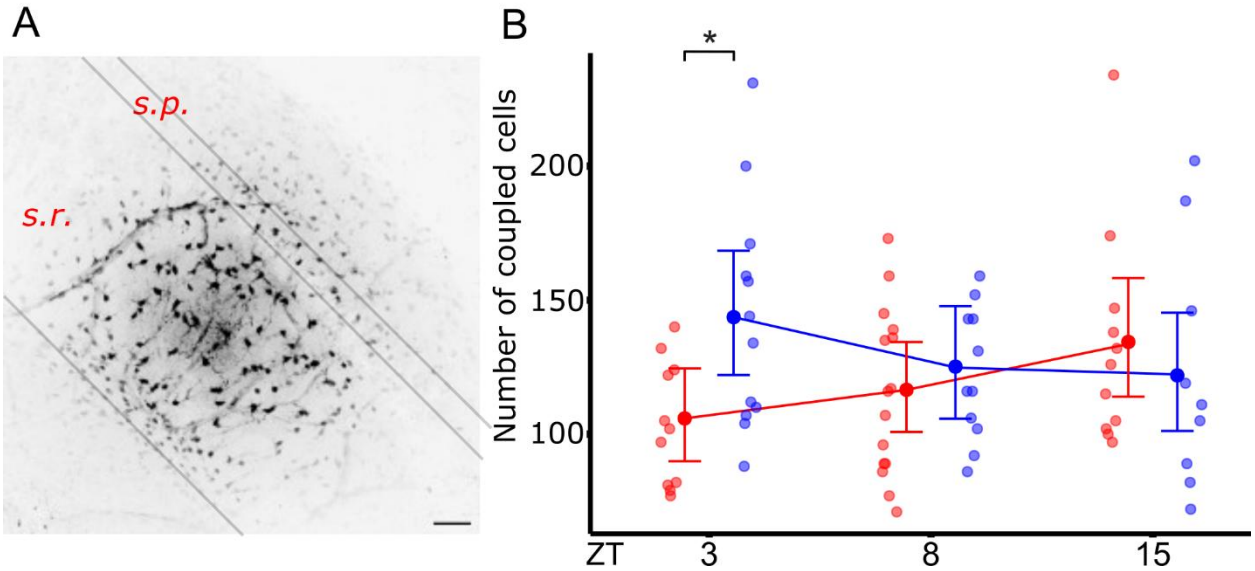

1109

1110

1111 Figure 3

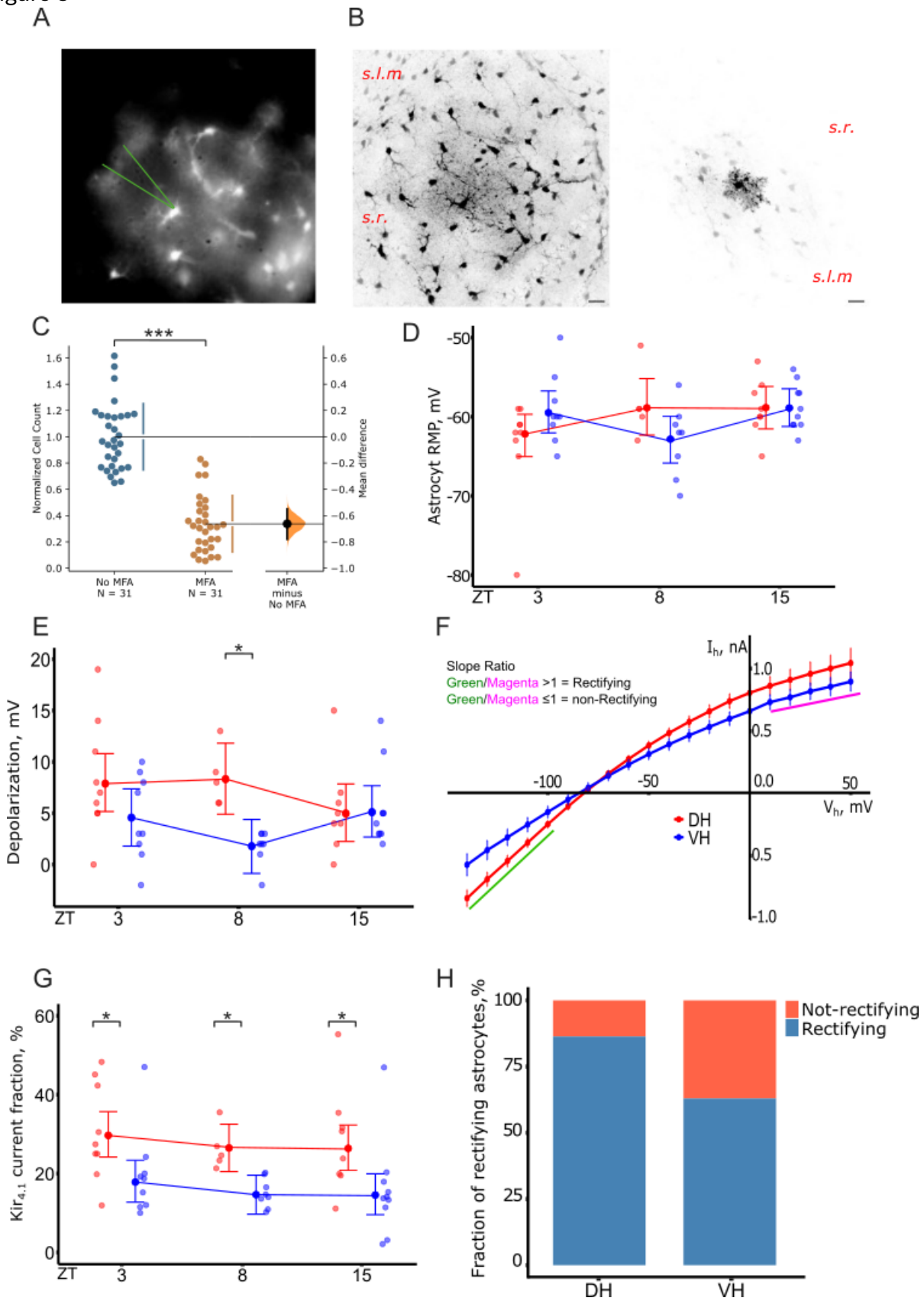

Figure 4

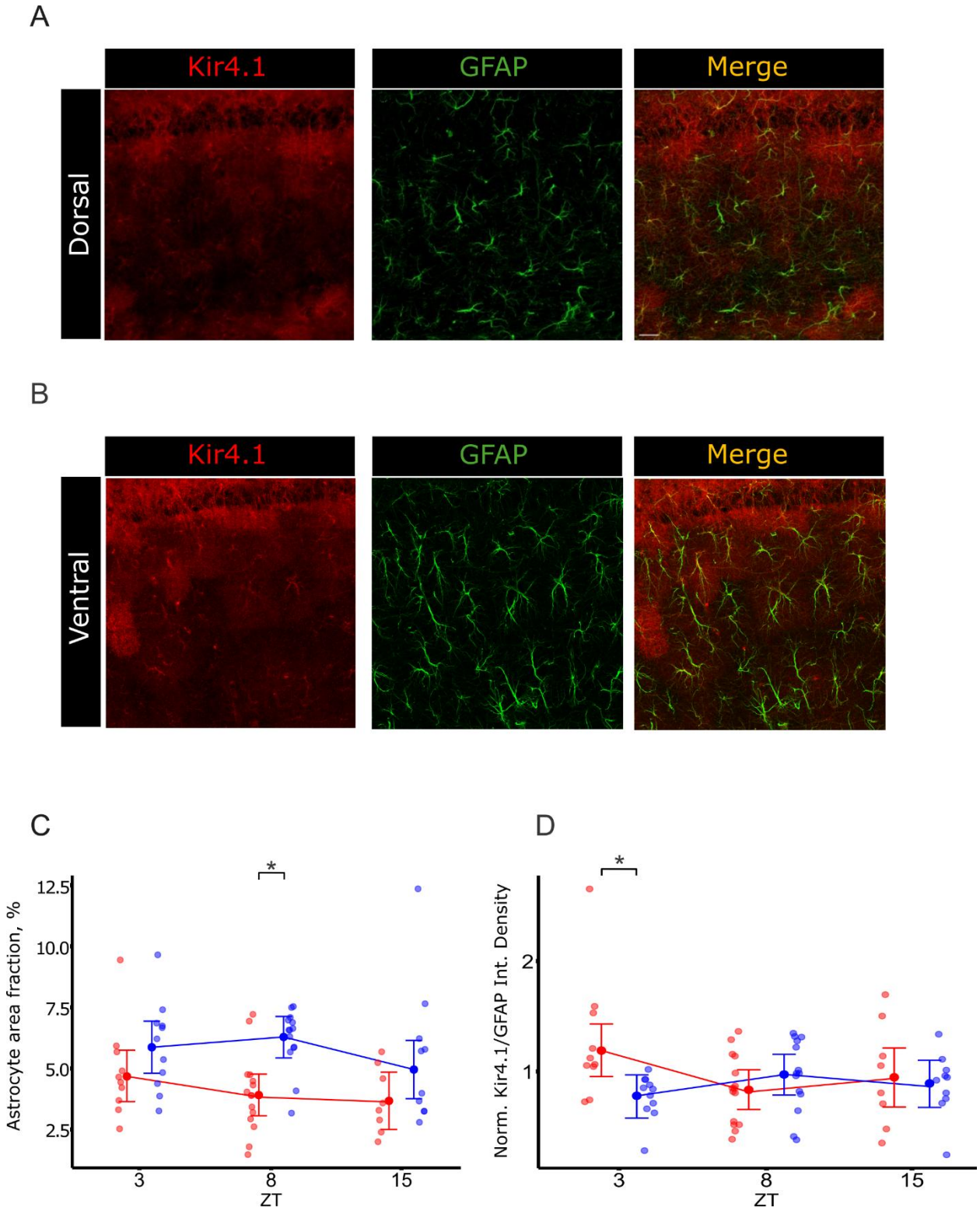
A
Kir4.1
GFAP
Merge
Dorsal
B
Kir4.1
GFAP
Merge
Ventral
C
*
Astrocyte area fraction, %
12.5
10.0
7.5
5.0
2.5
3
8
15
ZT
D
*
Norm. Kir4.1/GFAP Int. Density
2
1
3
8
15
ZT
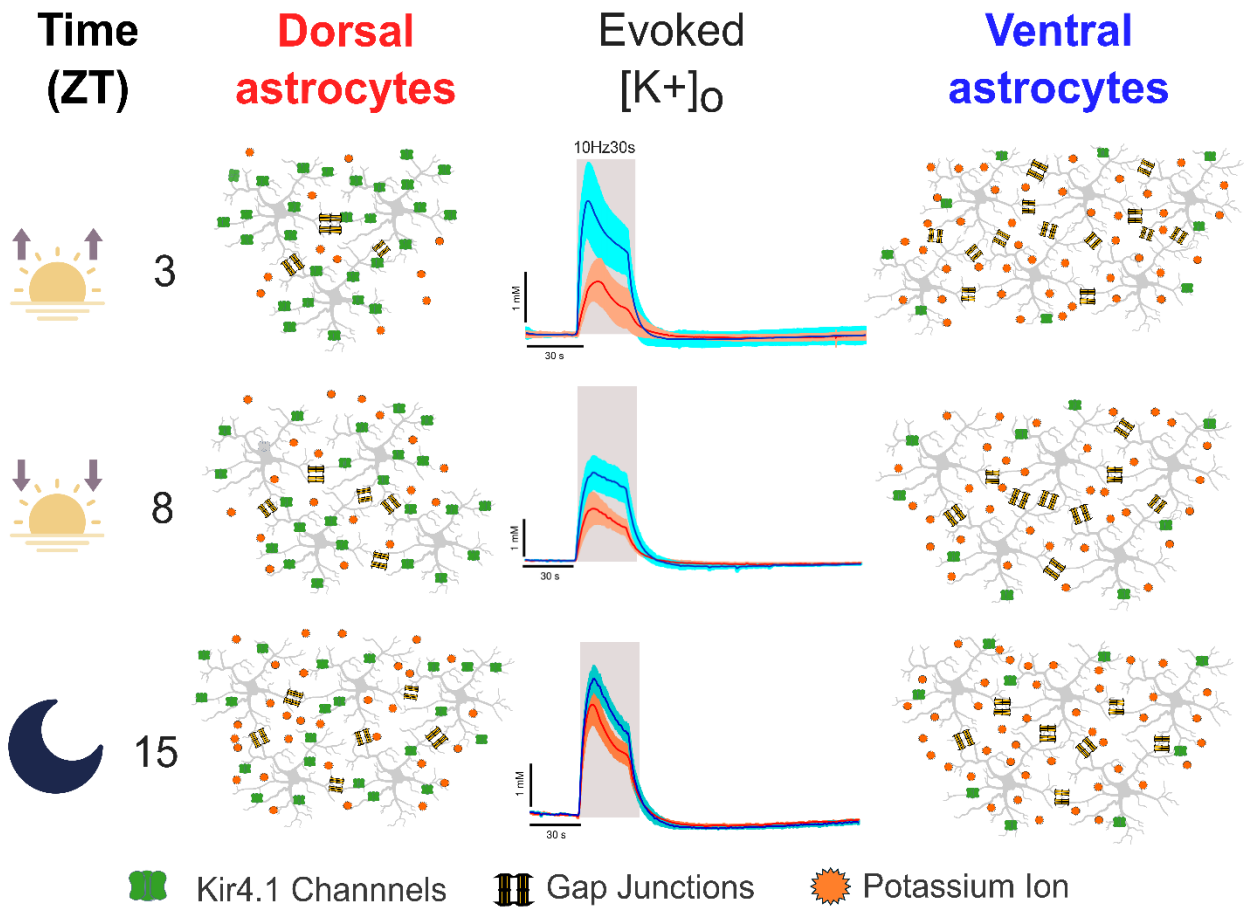
1114 Figure 5